Geochimica et Cosmochimica Acta 389 (2025) 186–199

Contents lists available at ScienceDirect

Geochimica et Cosmochimica Acta

journal homepage: www.elsevier.com/locate/gca

Modern oceanic cycle of beryllium isotopes assessed using a data-constrained biogeochemical model

Kai Deng [a,b,*], Gregory F. de Souza [b], Jianghui Du [c,b]

[a] State Key Laboratory of Marine Geology, Tongji University, 200092 Shanghai, China
[b] Institute of Geochemistry and Petrology, Department of Earth and Planetary Sciences, ETH Zurich, Clausiusstrasse 25, 8092 Zurich, Switzerland
[c] The Key Laboratory of Orogenic Belts and Crustal Evolution, MOE, School of Earth and Space Sciences, Peking University, 100871 Beijing, China

ARTICLE INFO

Associate editor: Tristan J. Horner

Keywords:
$^{10}Be/^{9}Be$
Continental input
Benthic process
Particle scavenging
Ocean circulation

ABSTRACT

Beryllium isotopes (stable ^{9}Be and cosmogenic meteoric ^{10}Be) enter the oceans through distinct pathways – i.e., from the continents and the atmosphere respectively – and display non-conservative behaviour in seawater. This isotope system has served as a powerful tool for quantifying a variety of processes, including geomagnetism, sedimentation, continental input, and ocean circulation. However, processes at land–ocean boundaries and within the ocean interior may either amplify or buffer the seawater isotope response to environmental changes. In the last decade, substantial effort has been invested in understanding external sources and internal cycling of Be isotopes, offering an excellent opportunity to revisit their modern oceanic cycle. Here, we investigate the controls on the modern oceanic cycling of Be isotopes using a three-dimensional ocean model, constrained by observational data on input fluxes and water-column distributions of ^{9}Be and ^{10}Be. In addition to modelling the previously known controls, we highlight the key role of marine benthic fluxes and scavenging onto particulate organic matter and opal in determining the mass balance and spatial distribution of Be isotopes. Inter-basin Be transport by the circulation is less important than external inputs at continent/atmosphere–ocean boundaries, except in the South Pacific. Therefore, the distribution of seawater $^{10}Be/^{9}Be$ ratios largely reflects that of the external inputs in most basins in the modern ocean. Finally, we apply our data-constrained mechanistic model to test the sensitivity of basin-wide $^{10}Be/^{9}Be$ ratios to changes of external sources and internal cycling. This analysis shows that seawater $^{10}Be/^{9}Be$ ratios are to some extent buffered against changes in continental denudation. For example, a 50 % decrease in denudation rates results in a 13–48 % increase in ocean-wide $^{10}Be/^{9}Be$ ratios. Moreover, the interplay between particle scavenging and ocean circulation can cause divergent responses in $^{10}Be/^{9}Be$ ratios in different basins. Weaker scavenging (e.g., 50 % decrease in intensity) would increase the homogenising effect of ocean circulation, making North Atlantic and North Pacific $^{10}Be/^{9}Be$ ratios converge (~20 % change in isotope ratios). The mechanistic understanding developed from this Be cycling model provides important insights into the various applications of marine Be isotopes, and offers additional tools to assess the causes of spatio-temporal Be isotope variations. We also identify the key oceanic processes that require further constraints to achieve a complete understanding of Be cycling in the modern ocean and back through time.

1. Introduction

Beryllium (Be) is a particle-reactive element that exhibits non-conservative behaviour during its transport from sources to sinks in the oceans (Merrill et al., 1960; Measures and Edmond, 1983; Ku et al., 1990). The meteoric cosmogenic isotope ^{10}Be, with a half-life of 1.39 Myr (Chmeleff et al., 2010), is produced in the atmosphere through spallation reactions and is primarily delivered to the oceans via rainfall; in comparison, stable ^{9}Be is delivered to the oceans from continental sources (Kusakabe et al., 1987; von Blanckenburg et al., 1996). The ocean circulation can homogenise Be isotopes to some extent (Kusakabe et al., 1987; von Blanckenburg and Igel, 1999), and scavenging by diverse types of particulates removes seawater Be isotopes into the particulate phase (Ku et al., 1990; Chase et al., 2002). The residence time of Be isotopes in seawater (10^2-10^3 yrs) is significantly shorter than the global oceanic mixing time (Anderson et al., 1990; von Blanckenburg et al., 1996), leading to spatially heterogeneous concentrations of ^{10}Be and ^{9}Be in seawater (Fig. 1).

* Corresponding author.
E-mail address: kaideng@tongji.edu.cn (K. Deng).

https://doi.org/10.1016/j.gca.2024.10.025
Received 30 June 2024; Accepted 23 October 2024
Available online 28 October 2024
0016-7037/© 2024 Elsevier Ltd. All rights are reserved, including those for text and data mining, AI training, and similar technologies.

Consequently, seawater $^{10}Be/^{9}Be$ ratios are subject to changes in the input fluxes of individual isotopes at ocean boundaries and to internal cycling processes (Measures and Edmond, 1983; Ku et al., 1990), and have been used to track a wide array of oceanographic processes. Marine authigenic $^{10}Be/^{9}Be$ ratios have commonly been employed to reconstruct the geomagnetic field strength on millennial scales, given its influence on the primary cosmic ray flux and subsequent ^{10}Be production (Christl et al., 2010; Simon et al., 2018). On million-year scales, when temporal variability in ^{10}Be production is averaged out, the isotope ratio has been used for dating marine archives based on the known radioactive decay of ^{10}Be (Bourlès et al., 1989a; Frank et al., 1999; Yi et al., 2020). With production- and decay-related variations in ^{10}Be corrected, the isotope ratio can be used to track relative changes in the fluxes from continental input, considering the delivery of ^{9}Be from continents (Willenbring and von Blanckenburg, 2010; von Blanckenburg et al., 2015; Simon et al., 2016). Moreover, this powerful tool can monitor internal cycling processes in the oceans, including particle scavenging and ocean circulation, due to the strong particle affinity for Be and inter-basin differences in isotope ratios (von Blanckenburg and Igel, 1999; Kong and Zhou, 2021).

Despite the numerous applications of oceanic $^{10}Be/^{9}Be$ ratios, the decoupled supply pathways of both isotopes complicate the interpretation of this oceanographic proxy. It is well known that the source of ^{10}Be to the ocean is overwhelmingly dominated by atmospheric precipitation, with a minor contribution from dust deposition (Merrill et al., 1960; von Blanckenburg et al., 1996), and the spatio-temporal variations in ^{10}Be depositional fluxes are relatively well understood (Christl et al., 2010; Heikkilä et al., 2013). In comparison, the transfer of ^{9}Be at the land–ocean boundary and its mixing with ^{10}Be in the open ocean is the subject of ongoing debate (von Blanckenburg and Bouchez, 2014; Suhrhoff et al., 2019; Li et al., 2021; Deng et al., 2023; Wang et al., 2024). Importantly, the response of seawater $^{10}Be/^{9}Be$ ratios to various processes of interest depends on how this transfer and mixing process is considered to happen, and thus on its parameterisation in models. Mass balance models can largely reproduce the difference in $^{10}Be/^{9}Be$ ratios between ocean basins if the continent-derived ^{9}Be flux is the major oceanic source and scales with continental denudation as shown by von Blanckenburg and Bouchez (2014). Nevertheless, the transfer efficiency of dissolved and particle-bound ^{9}Be across the continent-ocean interface to the open ocean (ϕ_{del}, where "del" denotes "delivery") was then considered as a tuning parameter in the model due to limited understanding of this process. The global value of ϕ_{del} was calculated to be 6.3 % to satisfy the mass balance of Be isotopes in the oceans (von Blanckenburg and Bouchez, 2014). This highlighted the need for more detailed observational constraints on the delivery of continent-sourced ^{9}Be for a mechanistic evaluation of oceanic Be cycling.

Recently, the delivery efficiency of riverine dissolved ^{9}Be in estuaries has been constrained based on a data compilation of estuarine transects (Suhrhoff et al., 2019); this efficiency (44 %) is higher than the ϕ_{del} value of the *total* continent-derived ^{9}Be input calculated by von Blanckenburg and Bouchez (2014; 6.3 %), which encompasses both dissolved and particulate phases. Using their own estimate of estuarine delivery efficiency, Suhrhoff et al. (2019) calculated that 64–147 tons/yr of dissolved ^{9}Be delivered by global rivers survives the coastal trap and enters the ocean. This figure is much lower than the oceanic ^{9}Be input (489 tons/year) required to yield the global deep ocean $^{10}Be/^{9}Be$ ratio, i.e., $\sim 8 \times 10^{-8}$ (von Blanckenburg and Bouchez, 2014). Consequently, it has been proposed that other sources, such as marine sediments, might drive important inputs of ^{9}Be to the ocean (Suhrhoff et al., 2019; von Blanckenburg et al., 2022; Wang et al., 2024). Indeed, the sediment source, i.e., a benthic flux of Be released during early marine diagenesis, has recently been quantified across diverse continental margins, and is much higher on continental shelves than in the deep sea (Deng et al., 2023). The early diagenetic release of Be from marine sediments to overlying seawater (Deng et al., 2023), together with the particle scavenging of dissolved Be at the continental margins (Anderson et al., 1990; Wittmann et al., 2017; Kong and Zhou, 2021), can be considered as a form of "boundary exchange" for Be isotopes, i.e., particle-dissolved exchange processes at the land–ocean contact (Lacan and Jeandel, 2005; Jeandel, 2016). Importantly, the oceanic ^{9}Be input derived from updated observational constraints on riverine dissolved loads, dust deposition, and benthic fluxes is balanced (within uncertainty) with the oceanic ^{9}Be output estimated using an independent approach (Deng et al., 2023) based on the ratio of the known global atmospheric ^{10}Be flux to the global average deep-sea $^{10}Be/^{9}Be$ ratio (von Blanckenburg et al., 1996). Overall, substantial progress has recently been made in constraining the effect of diverse processes, e.g., external inputs and internal cycling, on seawater Be isotopes. It is thus timely to revisit the modern oceanic cycle of Be isotopes by integrating the up-to-date observational constraints into a mechanistic and spatially-resolved framework.

In this study, we investigate the controlling processes in the modern oceanic Be cycle using a three-dimensional ocean biogeochemical model of Be isotope cycling coupled to a data-constrained physical circulation model (OCIM; DeVries, 2014). The Be-cycling model is driven by up-to-date data constraints on the sources of ^{10}Be and ^{9}Be to the ocean, and tested against a compilation of water-column observational dataset of Be isotopes from the literature. This spatially-resolved and data-

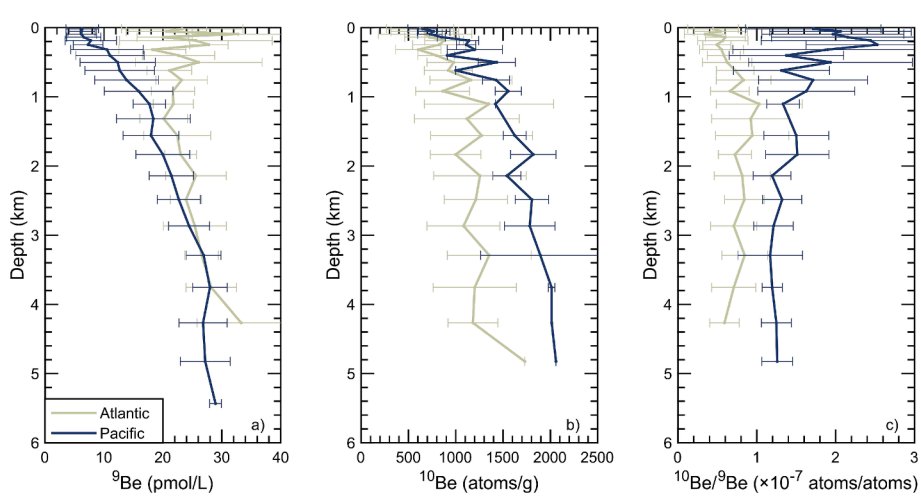

Fig. 1. Depth profiles of dissolved beryllium isotopes in the Atlantic and Pacific Oceans. Thick lines and error bars indicate average values and one standard deviation of the observations. In general, [^{9}Be] (a) and [^{10}Be] (b) increase with water depth, while $^{10}Be/^{9}Be$ ratios (c) are relatively constant. The Atlantic $^{10}Be/^{9}Be$ ratio is lower than that in the Pacific. Data sources are provided in the Supplementary Dataset.

constrained model also allows us to quantify the sensitivity of $^{10}Be/^{9}Be$ ratios to changes in external forcing and internal cycling, which provides valuable insights into the interpretation of seawater and authigenic $^{10}Be/^{9}Be$ ratios. Specifically, our key objectives are: (1) to quantify the role of individual ^{9}Be sources to the ocean, especially marine benthic fluxes and riverine dissolved loads; (2) to determine the primary scavenging agents globally, while also assessing the importance of ocean circulation in determining the distribution of Be isotopes; (3) to explore the sensitivity of seawater Be isotope ratios in individual basins to environmental changes.

2. Methods

2.1. The framework of the Be isotope ocean biogeochemical model

We apply an ocean biogeochemical modelling framework (AWESOME OCIM; John et al., 2020) to simulate the distributions of Be isotopes in the modern ocean. This MATLAB-based modelling tool applies the transport-matrix method (TMM) and a data-constrained estimate of the modern ocean circulation. The circulation is represented by a transport matrix (OCIM v1.0) derived from an ocean model constrained by observations, including temperature, salinity, chlorofluorocarbons, and radiocarbon (DeVries, 2014). The resolution of this model is 2° × 2° horizontally with 24 depth levels. The physical model is coupled to a biogeochemical model that simulates spatially-resolved sources, sinks and particle scavenging of Be isotopes. The equilibrium solution to this coupled model can be calculated by matrix inversion, providing high computational efficiency compared to online ocean general circulation models (John et al., 2020).

The general equation describing the evolution of the tracer concentration (C; [^{10}Be] or [^{9}Be]) is:

$$\frac{dC}{dt} = \sum_{i=1}^{N_s} S_{r,i} - T_{circ} \times C - J_{scav}(C) \quad (1)$$

where $\frac{dC}{dt}$ equals to zero at steady state, N_s is the number of external sources (S_r) of Be isotopes (Section 2.2), T_{circ} is the advection–diffusion transport matrix from the OCIM (DeVries, 2014), and J_{scav} is the C-dependent downward transport flux of Be isotopes by particulate scavenging (Section 2.3).

2.2. Oceanic sources of Be isotopes

In the model, cosmogenic ^{10}Be and stable ^{9}Be are treated as two independent tracers, similar to the isotope modelling approach from the original framework (John et al., 2020). Each source of Be isotopes is prescribed (Fig. 2) from data constraints, following the recently updated oceanic Be isotope budget of Deng et al. (2023).

2.2.1. Oceanic ^{9}Be sources

Simulated oceanic sources of ^{9}Be include riverine dissolved load, dust deposition and marine benthic fluxes (Fig. 2). We implement the riverine dissolved source of ^{9}Be using the river database compiled by Milliman and Farnsworth (2011), which includes outlet locations and water discharge data (n = 1258). Each river outlet is assigned to the nearest surface ocean grid cell at the continent-ocean boundary. The water discharge of each river in the database is multiplied by a uniform scaling factor so that the total water discharge of all rivers matches with the global water discharge estimate, i.e., 3.6 × 10^4 km^3/yr (Milliman and Farnsworth, 2011). Following the simplifying approach of Pasquier et al. (2022), we assume that rivers bear the same concentration of ^{9}Be ($[^{9}Be]_{riv}$ = 514 ± 104 pmol/L; post-estuarine removal). This figure is calculated as the product of the water-discharge-weighted concentration (1167 ± 237 pmol/L) from a global compilation of riverine data (Deng et al., 2023) and the average estuarine transmission efficiency (44 %) of ^{9}Be (Suhrhoff et al., 2019). The assumption of a uniform $[^{9}Be]_{riv}$ may lead to bias in modelling seawater $^{10}Be/^{9}Be$ ratios near the coast, but its effect is minor in the open ocean where seawater Be isotopes have been analysed and used for model evaluation. The ^{9}Be flux of each river is the product of $[^{9}Be]_{riv}$ and its water discharge, leading to a total effective riverine dissolved ^{9}Be input to the oceans of 1.8 ± 0.4 × 10^7 mol/yr.

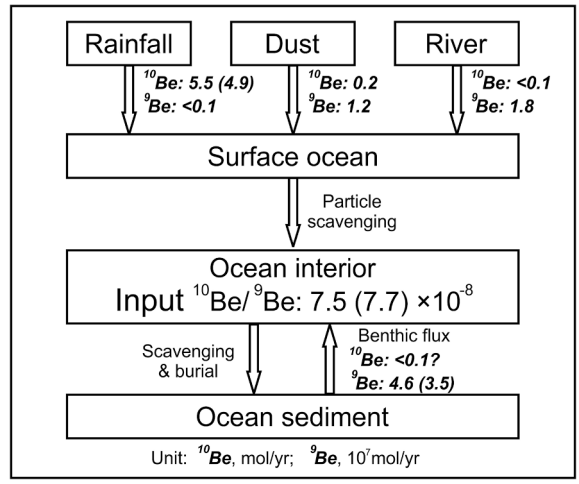

Fig. 2. Schematic plot of oceanic sources and sinks of Be isotopes in the model. Each process is spatially resolved and the total flux is shown here. The detailed parameterisation is described in Section 2. The surface ocean here indicates the topmost layer of the ocean in the model (depth: 0–36 m), and the ocean interior indicates all the other layers below. The input $^{10}Be/^{9}Be$ ratio indicates the ratio of the total ^{10}Be input to the total ^{9}Be input used in the model. The numbers outside the parentheses indicate the average values of individual sources used in the model Scenarios 1–5 in Table 1; the numbers inside the parentheses are the optimised values in a model scenario that considers the uncertainty of each (Scenario 10 in Table 1).

Atmospheric dust deposition delivers ^{9}Be to surface ocean grid cells (depth: 0–36 m), and a constant soluble fraction of dust ^{9}Be is released as dissolved ^{9}Be. A two-dimensional (2-D) mineral dust deposition field (in g/m^2/yr) is implemented in AWESOME OCIM (John et al., 2020) and described in a previous study (Chien et al., 2016). We assume that the Be concentration in dust is the same as that of the upper continental crust (2.1 μ g/g; Rudnick and Gao, 2003), and adopt a soluble fraction of dust ^{9}Be of 9 % (Brown et al., 1992). Based on the mean solubility of different metals (~5 to ~ 10 %; Duce et al., 1991), we estimate an approximate absolute uncertainty of 4 %. The resulting total dust ^{9}Be input, calculated as the product of dust deposition flux, dust ^{9}Be concentration and the soluble fraction of dust ^{9}Be, is 1.2 ± 0.5 × 10^7 mol/yr in this model.

The benthic ^{9}Be source represents the marine diagenetic release of particulate-bound Be from sediment pore-water to the water column (von Blanckenburg et al., 2022; Deng et al., 2023). Such a marine benthic flux has been invoked as an important oceanic source for many other trace metals, e.g., Fe, Mn and Nd (Elrod et al., 2004; McManus et al., 2012; Abbott et al., 2015; Dale et al., 2015; Deng et al., 2022). We parameterise this benthic ^{9}Be source following the strategy described in Deng et al. (2023). Benthic Be fluxes are considered to be depth-dependent and separated into three categories: 140 ± 107 pmol/cm^2/yr on continental shelves (0–0.2 km), 2.9 ± 0.3 pmol/cm^2/yr at 0.2–4 km, and 1.4 ± 0.2 pmol/cm^2/yr at > 4 km (Bourlès et al., 1989b; Deng et al., 2023). The flux within each water-depth interval is constrained by pore-water ^{9}Be measurements across diverse marine environments (range of water depths: 6–4910 m; Deng et al., 2023). The decrease in benthic fluxes with water depth can be explained by e.g., fast advective porewater-seawater exchange and strong Mn-Fe redox cycling on the shelves (Deng et al., 2023). Given the relatively coarse spatial resolution of OCIM (2° × 2°), seafloor bathymetry in the model is not properly represented. Hence, to obtain a more realistic sub-grid bathymetry for benthic ^{9}Be flux calculation, we calculate the actual seafloor area in each

ocean grid cell based on high-resolution (1 arc-minute) global bathymetry ETOPO1 (Amante and Eakins, 2009). In short, we assign the seafloor area in ETOPO1 to the nearest ocean grid cells in the model based on the location information (latitude, longitude, and depth), similar to the approach adopted by Aumont et al. (2015). The adjusted seafloor area in the model (3.6×10^8 km^2) is the same as the value in ETOPO1. The benthic ^{9}Be input (mol/yr) in each ocean cell is calculated as the product of the benthic ^{9}Be release rate at a given depth (mol/m^2/yr) and the seafloor area (m^2) derived from ETOPO1. The resulting global benthic ^{9}Be input is $4.6 \pm 3.0 \times 10^7$ mol/yr, representing the largest ^{9}Be source in the model.

2.2.2. Oceanic ^{10}Be sources

The major ^{10}Be sources to the ocean include atmospheric wet deposition (rainfall) and eolian dust, and are delivered to surface ocean grid cells. The riverine dissolved input is likely very small in magnitude (< 0.01 mol/yr) and thus neglected (Deng et al., 2023). This small magnitude can be explained by two reasons. First, the atmosphere-sourced ^{10}Be delivered to the continents mainly adsorbs to the particulate phase in rivers, due to its high particle affinity (You et al., 1989) and high particle concentrations in rivers (Milliman and Farnsworth, 2011); second, the effect of the estuarine traps (Suhrhoff et al., 2019) further reduces the flux of riverine dissolved ^{10}Be entering the oceans. For the rainfall input, we use a 2-D meteoric ^{10}Be deposition field (in mol/m^2/yr) simulated by a general circulation model. This atmospheric model was run twice under contrasting conditions of industrial and pre-industrial aerosol and greenhouse gas loading using modern solar modulation factor, i.e., Phi (Heikkilä and von Blanckenburg, 2015), and then results of both model scenarios are averaged. We did not take the model results that were further normalised to the Holocene-average Phi in Heikkilä and von Blanckenburg (2015), as our focus is on modern oceanic Be cycling and the oceanic residence time of Be is short. The use of a Holocene-averaged production rate would lead to a slightly higher ^{10}Be input (by ~ 20 %; Deng et al., 2020). The global rainfall ^{10}Be input to the oceans is 5.5 ± 1.3 mol/yr, the uncertainty of which represents the climate-dependent shifts in ^{10}Be delivery (Heikkilä and von Blanckenburg, 2015). The parameterisation of the dust ^{10}Be source is similar to that of dust ^{9}Be. It is based on the 2-D dust deposition field (in g/m^2/yr) implemented in the AWESOME OCIM (John et al., 2020), an assumption of 100 % solubility of dust ^{10}Be, and a dust [^{10}Be] ($2.1 \pm 0.7 \times 10^8$ atoms/g) derived from that in loess from the Chinese Loess Plateau (Shen et al., 2010). The dust [^{10}Be] also agrees well with that measured in another modern dust source area, i.e., Judean Desert (Belmaker et al., 2008). The global dust ^{10}Be input to the oceans is 0.20 ± 0.07 mol/yr in the model.

We also perform a sensitivity test on the potential benthic ^{10}Be source despite the fact that no pore-water ^{10}Be data are available. We assume that the benthic ^{10}Be flux is linked to the benthic ^{9}Be flux, which we multiply by a representative sediment authigenic ^{10}Be/^{9}Be ratio at each of the three water-depth intervals of our ^{9}Be flux parameterisation (details in the Supplementary Material). This sensitivity test shows that the benthic ^{10}Be input only accounts for a minor fraction (~6%) of the total ^{10}Be input, and the inclusion of this source does not reduce the model-data mismatch (Table 1). Given the lack of understanding of the benthic ^{10}Be source and its likely small magnitude, we do not include it in the discussion.

2.3. Particle scavenging and burial

2.3.1. Scavenging by diverse particles

Scavenging onto marine particles acts as the major internal cycling process for both Be isotopes (Kusakabe et al., 1982; Kusakabe et al., 1990), and is also the sole sink of both isotopes (i.e., through sediment burial) when particle-bound Be reaches the ocean bottom and is then removed from the model system. The total burial flux of Be isotopes must be identical to the total input at steady state. A key determinant of scavenging behaviour is the partition coefficient of Be between particulate and dissolved phases (K_d, in L/kg), which shows a wide range of < 10^5-10^6 (Chase et al., 2002; Grenier et al., 2023), depending on the particle composition and respective surface area. Particle affinity for Be increases with the proportion of biogenic silica (opal) in the particles (Kretschmer et al., 2011), while affinity of carbonate-rich samples for Be is low (Chase et al., 2002). Likewise, results from laboratory experiments show that K_d values for either biogenic silica or lithogenic particles (terrestrial Al_2O_3) in seawater (~10^5) are much higher than that of $CaCO_3$ (<10^4), and that addition of organic compounds can lead to an increase of K_d for each particle type (10^5-10^6; Yang et al., 2015). Besides, although metal oxides (e.g., MnO_2) have been suggested to have strong

Table 1
Optimised model results for different scenarios for oceanic particle scavenging and for choices of sources.

No.	Scavenging scenario	*Misfit*	K_d ($\times 10^5$ L/kg)[a] POC	Opal	Lithogenic particles	$CaCO_3$	Mn oxide
1	POC & opal & lithogenic particles & $CaCO_3$[b]	35.3 %	6.2	4.4	15.3	0.5	
2	POC & opal[c]	35.5 %	6.6	5.1			
3	Lithogenic particles & $CaCO_3$	47.6 %			106.2	4.6	
4	POC & opal & Mn oxide[d]	33.8 %	6.9	4.5			75.6
5	POC & opal (non-rev.)[e]	65.5 %	10.6	0.0			
6	POC & opal (excl. dust input)[f]	36.4 %	6.1	4.8			
7	POC & opal (excl. riverine input)[f]	37.4 %	6.0	4.7			
8	POC & opal (excl. benthic input)[f]	49.7 %	5.2	4.8			
9	POC & opal (incl. benthic ^{10}Be)[g]	36.2 %	6.4	5.3			
10	**POC & opal (incl. source uncertainty)[h]**	**33.7 %**	**5.7**	**4.5**			

Note: a) The partition coefficient (K_d) is estimated from the optimised equilibrium scavenging constant (K). The K_d values of POC and opal fall within the range of bulk K_d values determined from sediment trap samples in the field, i.e., ~1–15 $\times 10^5$ L/kg (Chase et al., 2002).
b) The globally averaged depth profiles of particle concentrations for the four particle types are shown in Fig. S1 in the Supplementary Material.
c) This is the reference scenario in the sensitivity test on scavenging mechanisms and on choices of sources.
d) The Mn oxide field is predicted from a decision-tree regression model (Fig. S2) based on water-column particulate Mn oxide observations (GEOTRACES Intermediate Data Product Group, 2021).
e) This scenario represents non-reversible scavenging to POC and opal. All other scavenging scenarios are characterised by the adsorption–desorption process between particle-bound and dissolved Be.
f) For Scenarios 6–8, each of them adopts the same parameterisation of sources and sinks as the reference scenario, except the exclusion of one given source, such as dust ^{9}Be and ^{10}Be input, riverine ^{9}Be input, and benthic ^{9}Be input.
g) This scenario adopts the same parameterisation of sources and sinks as the reference scenario, except the addition of a benthic ^{10}Be source.
h) This scenario adopts the same parameterisation of sources and sinks as the reference scenario, but the uncertainty of each source has also been considered for model optimisation. Hence, the best-tuned fluxes of each source, as well as the K_d values, are slightly different compared to the reference scenario, where the flux of each source is considered to be constant as the respective average value. The model results using this scenario are adopted in the Section Discussion.

affinity for numerous trace metals (e.g., Ni, Co, and Pa), for Be the difference in K_d values between Mn-rich and Mn-poor sediments is relatively small, suggesting that the contribution of MnO_2 to Be scavenging may be minor (Balistrieri and Murray, 1986; Anderson et al., 1990). In general, the affinity for Be is distinct between particle types, but how the particle-specific scavenging process affects the large-scale distribution of Be isotopes remains unclear.

2.3.2. Parameterisation of particle scavenging

In the model, particle-bound Be isotopes are not explicitly simulated. Instead, the model takes a fraction of the dissolved Be pool in each grid cell as the scavenged Be that is delivered to the grid cell below at a given sinking velocity. Following previous studies on scavenging of particle-reactive elements (Bacon and Anderson, 1982; Siddall et al., 2008), we assume that dissolved and particle-bound Be interact via an equilibrium model. The proportion of the total Be that sinks out of one grid cell per year (S_p, in yr^{-1}) is described by (John et al., 2020):

$$S_p = K \times C_p \times w/h \tag{2}$$

where K is the equilibrium scavenging constant (m^3/mmol), calculated as the mole ratio of sinking [Be] (mmol/m^3) to total [Be] (mmol/m^3) per mmol/m^3 of particles, C_p is the concentration of a given type of particle in a grid cell (mmol/m^3), w is the settling velocity of the particle (m/yr), and h is the height of the grid cell (m). Parameters K, C_p, and w are all dependent on particle type. The total Be that sinks from a grid cell depends on both K and w, meaning that an increase of w by twofold will result in the same model result as that with a twofold increase of K (John et al., 2020). The empirical partition coefficient of Be (K_d) can be calculated in reasonable approximation from K as $K/M_p \times 10^6$ (when $K \ll 1$), where M_p is the molar weight (g/mmol) of a specific particle type (Lam et al., 2018). We omit isotope fractionation during scavenging and adopt the same K for ^{10}Be and ^{9}Be, because its effect is negligible (e.g., a relative difference less than few percent for the boron isotope system with a similar atomic mass and relative mass difference; Gaillardet and Lemarchand, 2018) compared to the large variations in ^{10}Be/^{9}Be ratios (> 10 folds) caused by distinct sources of individual isotopes (Kusakabe et al., 1990). The total flux of sinking ^{10}Be or ^{9}Be (J_{scav}, mmol/yr) at a given location can be calculated as:

$$J_{scav} = \sum_{i=1}^{N_p} (S_{p,i} \times C \times V) \tag{3}$$

where N_p is the number of particle types in the model, C (mmol/m^3) is the total concentration of ^{10}Be or ^{9}Be, and V (m^3) is the volume of the grid cell.

We consider four types of particles as potential scavenging agents of Be isotopes, including particulate organic carbon (POC), biogenic silica (opal), lithogenic particles and carbonate. A 3-D POC concentration field sourced from a global nutrient cycling model (Weber et al., 2018) is implemented in AWESOME OCIM (John et al., 2020). A settling velocity (w) of 1 km/yr is assigned to POC (Siddall et al., 2008). Three-dimensional concentration fields of opal, lithogenic particles (dust) and carbonate, and their respective settling velocities from the PISCES model (Aumont et al., 2015), are taken from van Hulten et al. (2018) and re-gridded for the model used here. For additional sensitivity tests (Table 1), we include other scavenging processes such as scavenging to Mn oxides and non-reversible scavenging to particles, meaning that dissolved elements, once adsorbed to particles, are transferred to the ocean bottom and removed from the model system.

On a large spatial scale, as the specific scavenging intensities of individual particle end-members are not well constrained (Anderson et al., 1990; Chase et al., 2002; Li, 2005), we treat the equilibrium scavenging constant (K) of each potential scavenging agent as an unknown. These parameter values are optimised by minimising the mismatch between the simulated distributions of both Be isotopes and water-column observations. These observations (^{9}Be: n = 899; ^{10}Be: n = 380), compiled from the literature (Raisbeck et al., 1979; Measures and Edmond, 1982, 1983; Kusakabe et al., 1987; Segl et al., 1987; Ku et al., 1990; Xu, 1994; Measures et al., 1996; Frank et al., 2002; Frank et al., 2009), cover three ocean basins: the Arctic, the Atlantic and the Pacific (Fig. 3). The compiled dataset is provided as a Supplementary Dataset, and the selection criteria for data used in model optimisation are described below.

2.4. Model optimisation

2.4.1. Optimising scavenging parameters

The equilibrium scavenging constants (K) of potential Be scavenging agents are the key unknown parameters in our simulations, for which the external sources of Be isotopes are prescribed from data constraints (as described in Section 2.2). We thus constrain the scavenging parameters by model optimisation towards open-ocean water column Be isotope data compiled from the literature (Fig. 3). The model is objectively optimised by minimising the model-observation mismatch, quantified using the following objective function:

$$Misfit = \sum_{j=1}^{N_{basin}} \frac{V_j}{V_{total}} \times \left(\frac{1}{2} \times \frac{\sqrt{\frac{\sum_{i=1}^{N_{obs,j}} \left([^{9}Be]_{obs,\ i,j} - [^{9}Be]_{mod,\ i,j} \right)^2}{N_{obs,j}}}}{[^{9}Be]_{obs,\ mean,j}} + \frac{1}{2} \times \frac{\sqrt{\frac{\sum_{i=1}^{N_{obs,j}} \left([^{9}Be]_{obs,\ i,j} - [^{10}Be]_{mod,\ i,j} \right)^2}{N_{obs,j}}}}{[^{10}Be]_{obs,\ mean,j}} \right) \tag{4}$$

Thus, the *Misfit* between model (mod) and observation (obs) is determined as the basin-volume-weighted, normalised root mean square deviation (NRMSD) of both Be isotopes. $N_{obs,j}$ is the number of observations (^{10}Be or ^{9}Be) in ocean basin j, and N_{basin} is the number of ocean basins where observations exist, i.e., the Arctic, the Atlantic and the Pacific. As oceanic ^{10}Be and ^{9}Be are modelled separately, the objective function depends on both tracers and the relative contribution of each tracer to this function is equal. The NRMSD of Be isotopes in each ocean basin is weighted by their ocean basin volume in order to reduce the bias resulting from the irregular spatial distribution of observations (Eisenring et al., 2022). In particular, the Arctic with a small volume (1.4 % of global ocean volume) plays a secondary role in the optimisation process compared to other large basins. The model optimisation is unconstrained, meaning that we prescribe no limits on the numerical values that the scavenging constants can take. The optimised scavenging constants are compared later with scarce measured values to assess their reliability. Additionally, for model optimisation, the following observations are excluded: 1) observations with incomplete location information (latitude, longitude and water depth); 2) observations at the coast-ocean boundary of the model, because the ocean circulation there may be less accurate, and the modelled values may be strongly

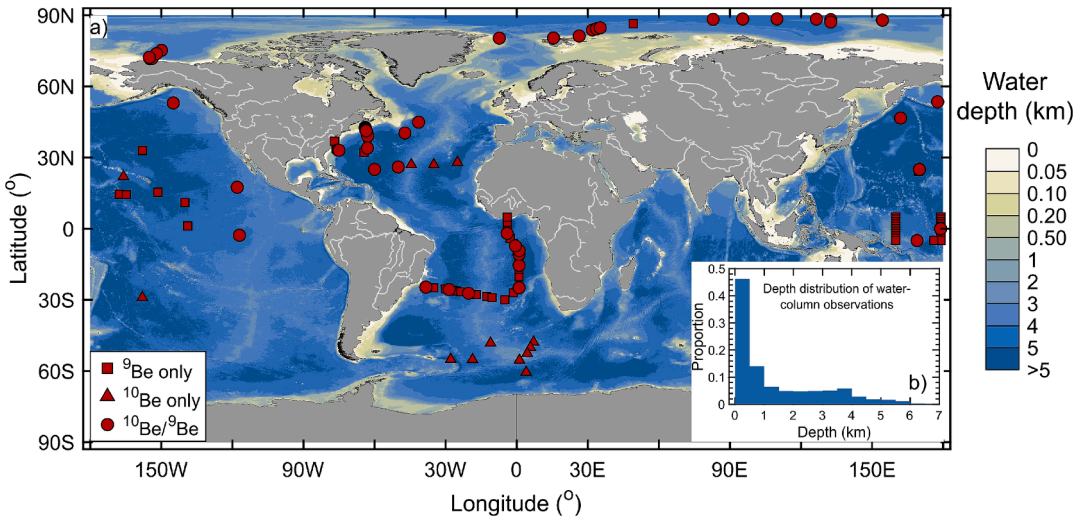

Fig. 3. Spatial distribution of Be isotope dataset compiled from the literature. A) Global bathymetric map with locations of water-column samples. B) The depth distribution of all compiled samples. Beryllium isotope data for these samples are provided in the Supplementary Dataset.

influenced by nearby point sources, such as rivers; 3) observations that fall into continent grid cells of the model. This results in the exclusion of ~ 24 % of the observations in total.

To minimise the objective function, we adopt the global optimisation algorithm in MATLAB that combines both functions Multistart and fmincon. In brief, the algorithm starts from a large number of initial points and attempts to find multiple local minima; many of them converge towards similar solutions with the smallest value of the objective function, and may be the global minimum, which is adopted as the best estimate. The optimisation process is run in parallel on the high-

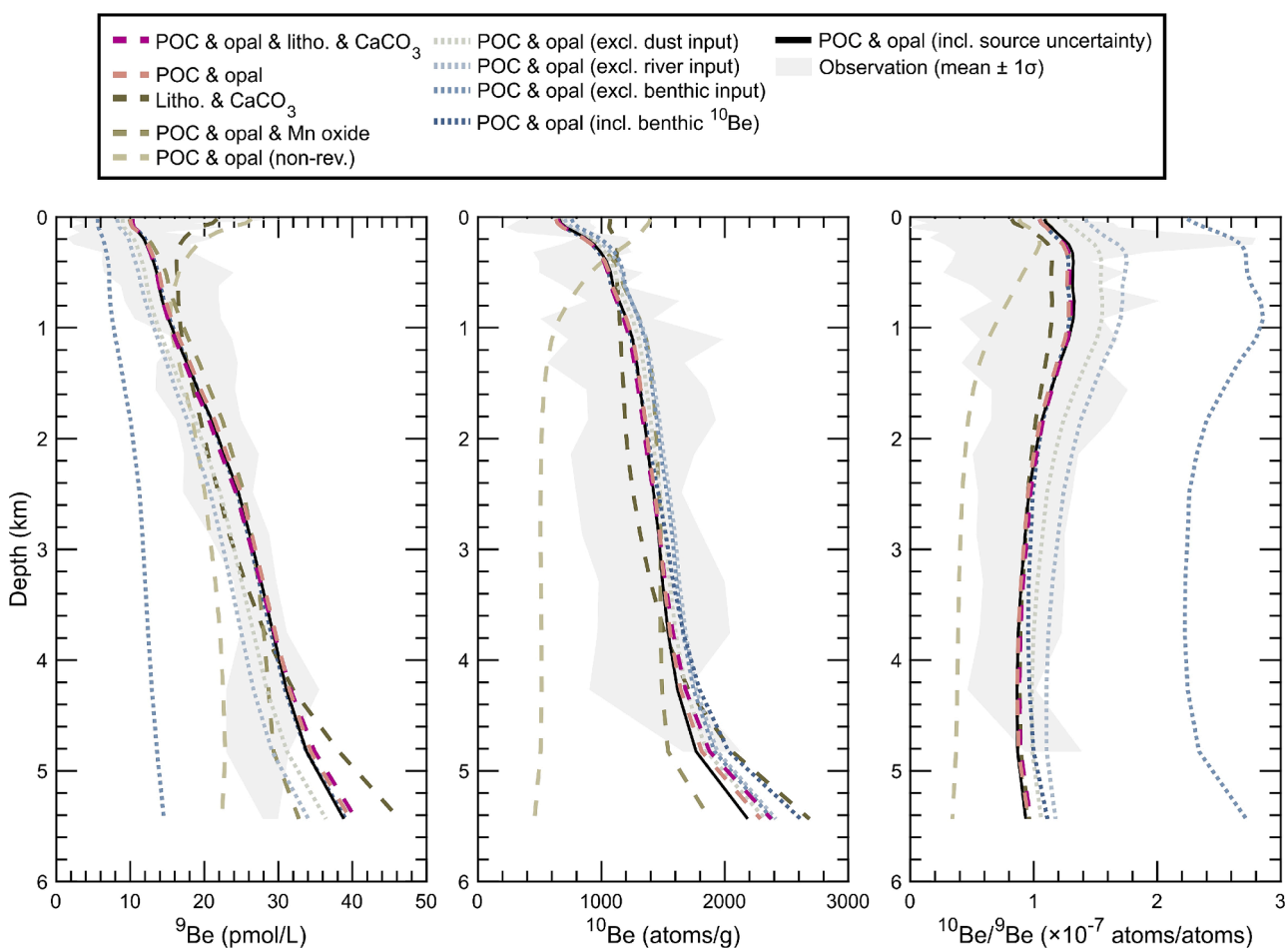

Fig. 4. Depth profiles of modelled globally averaged dissolved Be isotopes, with the minimum model-observation *Misfit* based on different scenarios for oceanic particle scavenging (dashed lines) and for choice of sources as a sensitivity analysis (dotted lines). The final optimised results used in the Section Discussion is shown as black lines. The details of each scenario are described in Table 1.

performance computing cluster Euler at ETH Zurich.

2.4.2. Additional considerations on source uncertainties

For model optimisations focusing on identification of the relevance of individual scavenging agents, each source of Be isotopes enumerated in Section 2.2 is set to its representative average flux. Once the dominant scavenging agents were determined, we additionally optimised the input flux of each source, within its uncertainty, together with the scavenging efficiency of selected particle types. While the optimisation of scavenging constants was unconstrained, we added a penalty constraint on the size of each Be source into the objective function (Pasquier et al., 2022), to prevent it from reaching unrealistic values during optimisation:

$$Misfit_p = Misfit - e_p \times \sum_{i=1}^{N_s} ln(P(S_{r,i})) \quad (5)$$

$Misfit_p$ is the observation-model mismatch that also considers the penalty constraints on Be sources, while *Misfit* is the NRMSD of Be isotopes (Eq. (4). The second term, i.e., the penalty constraint, is the sum of the negative log-likelihood, that is, $-\ln(P(S_r))$, of all Be sources. The probability (P) of each source (S_r) is described as a normal distribution (average ± standard deviation). Seven source terms ($N_s = 7$) are considered here: riverine dissolved ^{9}Be input, dust ^{9}Be input, benthic ^{9}Be input at 0–0.2 km, 0.2–4 km, and > 4 km, rainfall ^{10}Be input, and dust ^{10}Be input. Their average values and the standard deviations are constrained by literature data and provided in Section 2.2. The coefficient e_p (using a constant of 0.05 here) scales the effect of the penalty on $Misfit_p$ compared to the effect of *Misfit* (Eq. 4). During the optimisation process, the penalty increases if the magnitude of a source (S_r) moves away from its average value, which is data-constrained and considered to be representative. Hence, such changes in S_r can only be made during optimisation if the corresponding decrease in the model-observation mismatch of Be isotopes (*Misfit*) is larger. Based on Eq. (5), if the change in one source magnitude reaches one standard deviation, the NRMSD of Be isotopes must decrease by at least 2–3 % to obtain a lower $Misfit_p$.

3. Results

3.1. Determination of dominant scavenging agents

We determine the dominant particle types impacting the distribution of Be isotopes by testing the sensitivity of optimisation results to the choice of different scavenging agents (Table 1 and Fig. 4). This assessment shows that a combination of four major particle types (POC, opal, lithogenic particles and $CaCO_3$) can, to a large extent, reproduce the spatial distributions of both Be isotopes – i.e., the increase of [^{9}Be] and [^{10}Be] with depth, and a relatively constant ^{10}Be/^{9}Be ratio (Fig. 4). The residual model-data mismatch (*Misfit*: 35.3 %) can be ascribed to the representation of individual particle fields, regional-scale inaccuracies in the physical model, and/or the constants adopted in the parameterisation of particle scavenging and external sources.

Scavenging parameters resulting from this unconstrained model optimisation to seawater ^{10}Be/^{9}Be data are generally within the range of observations, ranging from 0.5 to 15.3 × 10^5 L/kg depending on particle type (Scenario 1 in Table 1). The scavenging agents that dominate the sinking Be flux on the global scale (~90 % on average) are POC and opal, based on Eq. (3) and optimised K values. The other two types of particles, i.e., lithogenic particles and $CaCO_3$, play only a minor role, and lead to a much larger *Misfit* when only these two types are chosen as scavenging agents (Table 1). Though $CaCO_3$ is a very important biogenic particle in the ocean, its adsorption capacity for Be is known to be much lower (e.g., K_d of < 10^4 L/kg) than that of POC or opal (10^5-10^6 L/kg; Chase et al., 2002; Yang et al., 2015). The median concentration of lithogenic particles is 1–2 orders of magnitude lower than other major particle types (Aumont et al., 2015), reducing their scavenging impact accordingly, given that its K_d for Be does not considerably exceed that of POC or opal (Scenario 1 in Table 1). Indeed, when optimised using only POC and opal as the scavenging agents, the model can still explain the spatial distribution of Be isotopes with a similar *Misfit* as when all four particle types are used (35.5 % versus 35.3 %; Table 1).

Furthermore, as Mn oxide is considered as a potential scavenging agent for certain particle-reactive metals, we also include it in a sensitivity test (Table 1). Since the distribution of particulate Mn oxides is poorly constrained (van Hulten et al., 2017), we generated a 3-D MnO_2 field using a tree-based regression model derived from sparsely observed Mn oxide data (GEOTRACES Intermediate Data Product Group, 2021) and several potential predictors with global coverage (Fig. S2 in the Supplementary Material). This field is a rough estimation and likely bears a large uncertainty, and is thus only applied in this sensitivity test. The results show that the addition of Mn oxide does not change the shape of the Be depth profiles, and only slightly reduces the model-observation *Misfit*, particularly at very great depths (Fig. 4). As such, Mn oxides may not play a dominant role in Be scavenging on a global scale. A robust evaluation of its effect will, however, rely on a comprehensive understanding of the global distribution of MnO_2 in the water column.

Given that scavenging to only POC and opal with optimised K_d values can reproduce the Be isotope distributions, we adopt only these two scavenging agents for further simulations. In this scenario (Scenario 2 in Table 1), POC acts as the dominant scavenging agent, with 77 % (on average) of particle-bound Be in the water column sorbed to POC. The partition coefficients for oceanic Be (K_d) derived from the optimised scavenging constants (Table 1) are estimated as ~ 7 × 10^5 L/kg for POC and ~ 5 × 10^5 L/kg for opal; our optimised K_d values, however, depend on the choice of w values in the model (John et al., 2020) and bear some uncertainties. Nevertheless, these K_d values fall within the wide range determined from sediment trap samples in the field, i.e., ~1–15 × 10^5 L/kg (Chase et al., 2002) and from laboratory adsorption experiments, i.e., 10^5-10^6 L/kg for a combination of SiO_2 and organic compounds (Yang et al., 2015). As the scavenging efficiency is the major tuning parameter in our model, it is encouraging that our model optimisation reproduces observed distributions of Be isotopes while also returning simulated K_d values that are overall consistent with observations (Fig. S3).

3.2. Comparison between the optimised model and observations

In the sensitivity tests on the scavenging agents above, the fluxes of individual sources were fixed to their average values (Fig. 2) during the optimisation process and indeed result in a small *Misfit* (Table 1). Nevertheless, considering that each source bears some uncertainties, we further fine-tune the model by optimising both the scavenging parameters for POC and opal, as well as the flux of each source within the given uncertainty (Eq. (5). The final optimised results are shown as Scenario 10 in Table 1, and produce a *Misfit* (33.7 %) that is slightly lower than that considering each source as a constant (35.5 %). The optimisation process tunes down the rainfall ^{10}Be input and the benthic ^{9}Be input on continental shelves by 12 % and 27 % respectively (Fig. 2), while other sources remain unchanged (<1% of difference). All model results shown hereafter are based on this model optimisation with optimised source magnitudes.

Simulated water-column [^{9}Be], [^{10}Be] and ^{10}Be/^{9}Be ratios are shown in Fig. 5 and compared to literature observations. Though ^{10}Be and ^{9}Be are treated as two independent tracers, and the isotope ratio is neither explicitly modelled nor explicitly included in the objective function driving model optimisation, the simulated distribution of ^{10}Be/^{9}Be is well correlated with observations ($R^2 = 0.75$). This result demonstrates the capability of our model to reproduce the spatial pattern of ^{10}Be/^{9}Be ratios over a range of around 2 orders of magnitude (10^{-8}-10^{-6} atoms/atoms).

The correlation between observed and modelled [^{9}Be] is weaker,

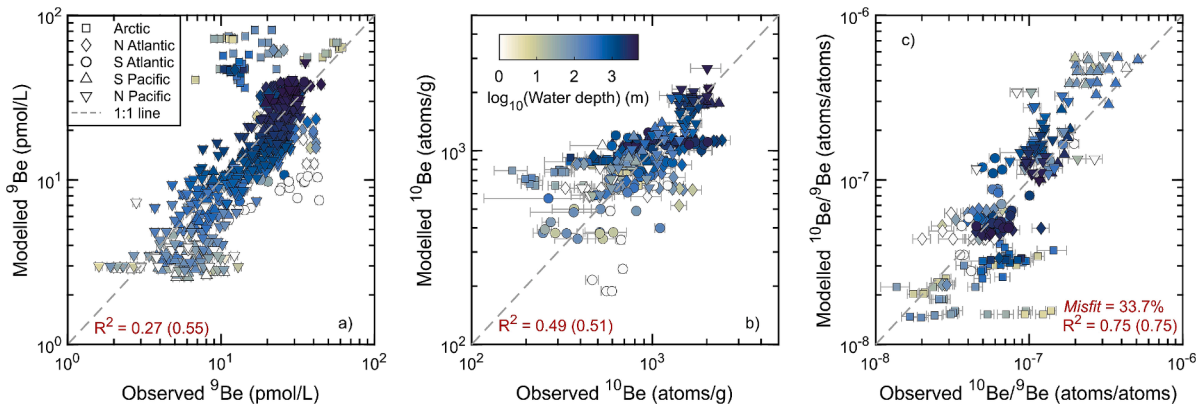

Fig. 5. Modelled vs. observed dissolved Be isotope data in the global oceans. Simulated [^{9}Be] (a), [^{10}Be] (b), and ^{10}Be/^{9}Be ratios (c) are derived from model Scenario 10, based on scavenging to POC and opal and optimised fluxes of individual sources. The symbols are colored by water depth. Error bars on observations are analytical errors, and those for [^{9}Be] (relative error: 5 %) are generally smaller than the symbols. The correlation coefficient (R^2) is calculated based on the entire dataset in each panel, using the linear scale. The numbers in parentheses (all ≥ 0.5) are the R^2 calculated excluding data for the Arctic, where the circulation pattern is poorly constrained and the inter-annual variability in certain trace metals is high. The Arctic with a small volume nonetheless plays a secondary role when calculating the basin volume weighted normalised root mean square deviation (NRMSD; Eq. 4) during model optimisation. All p values (with or without the Arctic dataset) are < 0.01. The model-observation *Misfit* (33.7 %) shown in c) is determined as the basin-volume-weighted NRMSD of [^{9}Be] and [^{10}Be].

partly because of the large model-observation mismatch in the Arctic (Fig. 5). There are two potential explanations for this mismatch. First, the ocean circulation in the Arctic is poorly constrained in the model due to patchy data coverage (DeVries and Primeau, 2011). Second, the Arctic, as a small ocean basin (1.4 % of global ocean volume) is more sensitive to short-term and regional-scale changes, such as inter-annual variability in river runoff (Charette et al., 2020). Indeed, the dissolved concentrations of trace metals with a short residence time (10^2-10^3 yrs) show large inter-annual variability in the shallow Arctic (Bundy et al., 2020), which may not be captured by our large-scale steady-state model. The model-observation correlation for ^{9}Be is improved ($R^2 = 0.55$) when the Arctic dataset is excluded. Likewise, the model-observation mismatch for [^{10}Be] is large in the Arctic, and the R^2 of modelled vs. observed [^{10}Be] in the non-Arctic dataset reaches 0.51.

4. Discussion

4.1. Features of the optimised oceanic Be cycle

Our optimised model of the oceanic Be cycle includes POC and opal as major scavenging agents, with source magnitudes optimised within a data-constrained range. The optimised total input fluxes of ^{10}Be (5.1 mol/yr) and ^{9}Be (6.6×10^7 mol/yr) set an input ^{10}Be/^{9}Be ratio of 7.7×10^{-8} (Fig. 2). Atmospheric wet deposition overwhelmingly dominates the ^{10}Be input (96 %), while benthic fluxes act as the major ^{9}Be source (54 %). Each Be source plays a role in determining the distribution of Be isotopes by enhancing the model-data agreement, as excluding any one of them during the optimisation of scavenging constants can result in a higher *Misfit* (Scenarios 6–8 in Table 1). In particular, excluding the benthic fluxes (the largest ^{9}Be source) leads to the highest *Misfit* as expected (Scenario 8). Following the previous Be model framework (von Blanckenburg and Bouchez, 2014), the sum of riverine dissolved load and shelf benthic fluxes at land–ocean interface (4.7×10^7 mol/yr) would indicate a global ϕ_{del} of 5.4 % in our model, falling within the estimated range by isotope mass balance (6.3 % ± 3.6 %; von Blanckenburg and Bouchez, 2014). Regarding the scavenging of Be isotopes to the seafloor (output), the ^{10}Be/^{9}Be ratio in the global output equals to that of the input (Fig. 6), as required for isotope mass balance. The rate of Be supplied by scavenging per unit area to the seafloor of the shelf ($\leq$0.2 km depth) is much higher than the global average output rate for both ^{10}Be (approximately twofold) and ^{9}Be (approximately eightfold), reflecting the enhanced scavenging at the continental margins due to higher particle concentrations (Anderson et al., 1990).

The optimised model reproduces not only the increase in [^{10}Be] and [^{9}Be] with water depth (Fig. 4 and Fig. S4), but also the observed increase in ^{10}Be/^{9}Be ratios from the Atlantic to the Pacific (Fig. 6 and Fig. 7). The increase in [^{10}Be] and [^{9}Be] with water depth can be reproduced when scavenging is parameterised as the adsorption–desorption process between particle-bound and dissolved Be (Bacon and Anderson, 1982; Siddall et al., 2008), but not as a non-reversible scavenging process (Fig. 4). Specifically, non-reversible particle scavenging would lead to [^{9}Be] in the deep sea that are much lower than observations; resolving this discrepancy would require a large benthic flux in the abyssal basins. In contrast, existing observations show much smaller benthic fluxes at greater depths (Deng et al., 2023). In comparison, the scavenging scheme we adopted (Scenario 10) can

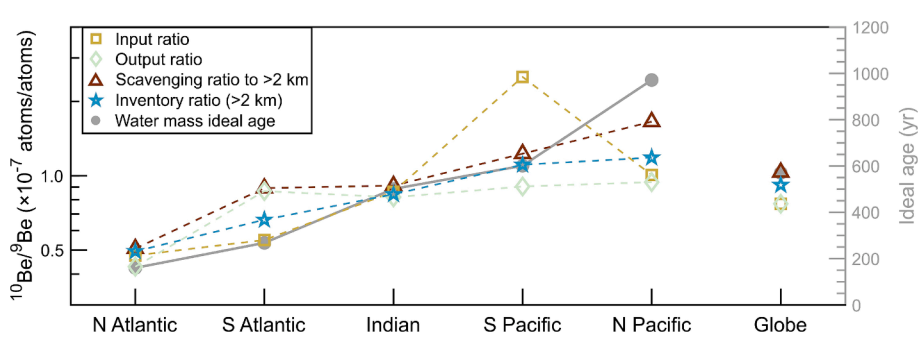

Fig. 6. Beryllium isotope ratios of oceanic inputs, outputs, sinking particulates, and deep-sea (>2 km) inventories in the optimised model (Scenario 10). The mean ideal age of each water mass in OCIM is also shown.

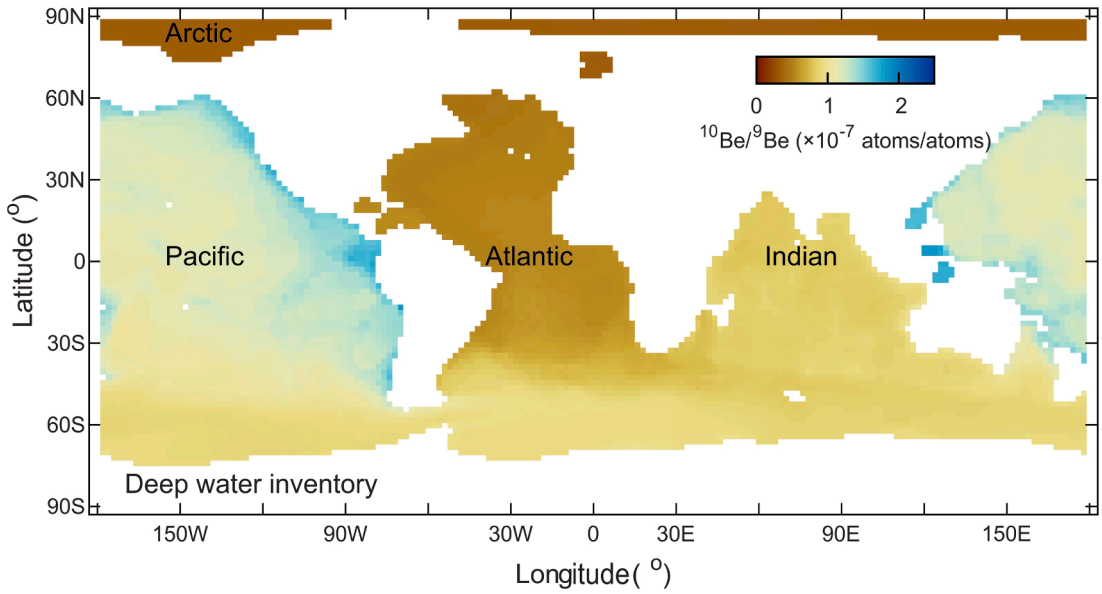

Fig. 7. Global distribution of modelled seawater $^{10}Be/^{9}Be$ ratios in the deep ocean. The inventory of each Be isotope is integrated over the deep water depths (>2 km), and the inventory ratio of ^{10}Be to ^{9}Be is shown. The isotope ratios for the inventory integrated over the full water column is shown in Fig. S5. The model results are based on Scenario 10 in Table 1.

lead to strong scavenging of dissolved Be in shallow waters and release of particle-bound Be at depth, driven by the decrease in particulate concentrations with depth due to primary production near the surface and remineralisation at depth (Aumont et al., 2015).

At the basin scale, the $^{10}Be/^{9}Be$ ratios of external inputs increase from the Atlantic to the Pacific (Fig. 6), with the highest ratio in the South Pacific, due to a large surface area for ^{10}Be deposition and a relatively small ^{9}Be input. A similar inter-basin trend is observed in both the $^{10}Be/^{9}Be$ ratios of the sediment burial (output), and the particulate scavenging flux into the deep ocean, albeit at a different magnitude due to the operation of internal cycling processes. The $^{10}Be/^{9}Be$ ratio of the deep-sea (>2 km) inventory represents the integrated effect of deep ocean circulation and scavenging supply to the deep ocean, and thus differs from the scavenged $^{10}Be/^{9}Be$ in individual basins (Fig. 6). Overall, the increase in deep-sea $^{10}Be/^{9}Be$ ratios along the deep-water circulation pathway, as shown in both observations and the model (Fig. 8), is largely consistent with the higher input ratio in the Pacific compared to the Atlantic. This implies that the main control on the differing $^{10}Be/^{9}Be$ ratios of these two basins is the difference in the $^{10}Be/^{9}Be$ ratios of external sources, with small differences in ratios between inputs and deep-sea inventories resulting from the effect of internal cycling processes (scavenging and circulation), as discussed below.

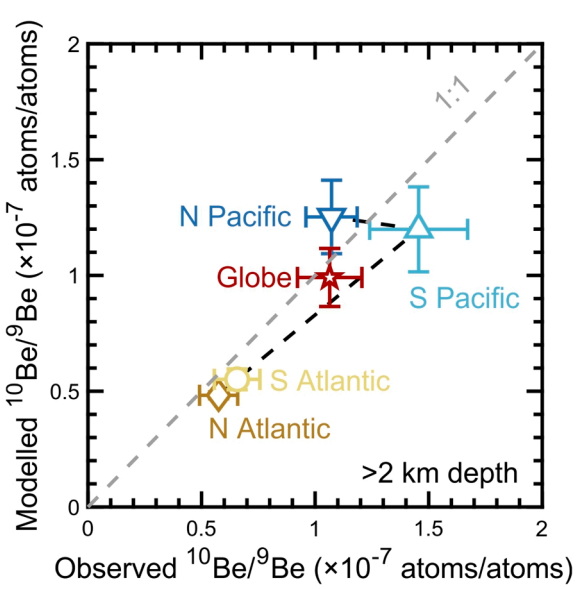

Fig. 8. Comparison between modelled and observed basin-averaged, deep-sea (>2 km) $^{10}Be/^{9}Be$ ratios. Model results are only included from grid cells within which observations exist. Error bars for each basin indicate one standard deviation. The black dashed line indicates the deep-sea circulation pathway. The "Globe" data indicates the basin-volume weighted average ratio and the basin-volume weighted standard deviation.

4.2. Role of ocean circulation in the modern oceanic Be cycle

The increase of deep-sea $^{10}Be/^{9}Be$ ratios along the deep water circulation pathway (Fig. 6) appears to mimic the increase in water mass ideal age, that is, the time since its last contact with the ocean surface (Thiele and Sarmiento, 1990). Nevertheless, the similarity between the input $^{10}Be/^{9}Be$ ratios (no circulation effect) and deep-sea $^{10}Be/^{9}Be$ ratios (which are affected by external input, circulation and scavenging) in most basins (Fig. 6) suggests a relatively weak impact of inter-basin circulation (compared to external inputs) in the modern ocean. It is also consistent with the short residence time of Be isotopes (400–600 yrs in the model) relative to the timescale of the global circulation (~1400 yrs; Khatiwala et al., 2012).

To quantify the importance of circulation-related Be transport in each ocean basin, integrated over full depths, in comparison to external inputs into the entire basin, we calculate the difference between basin-wide outputs and inputs (Fig. 9) as the net circulation-related flux. This flux reflects the net effect of Be import (and export) from (and to) adjacent basins on the basin-wide inventory. Compared to previous estimates of the net effect of water circulation on seawater [^{10}Be] (von Blanckenburg et al., 1996), which assumed a uniform ^{10}Be depositional flux and residence time worldwide, our spatially-resolved modelling technique distinguishes between the contributions from external inputs and water circulation in each basin; furthermore, it enables us to resolve the effects on ^{10}Be and ^{9}Be individually (Fig. 9). Our calculation shows that the circulation indeed exports both ^{9}Be and ^{10}Be from the North Atlantic and the North Pacific, and imports both isotopes to the Indian Ocean. Nevertheless, the ratio of transport fluxes to basin-wide external

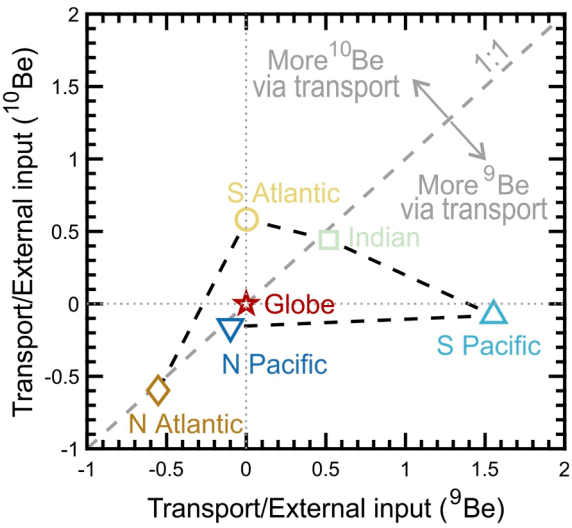

Fig. 9. Net circulation-related fluxes of Be isotopes to individual basins relative to the basin-wide external inputs. Positive numbers mean the transport of Be isotopes into the given basin. The black dashed line indicates the deep-sea circulation pathway. Symbols close to the 1:1 line indicate that the effect of water transport does not cause significant deviation of the basin-wide ^{10}Be/^{9}Be ratios from external inputs.

input for ^{10}Be is similar to that for ^{9}Be in these basins. Hence, although the magnitude of the circulation-related flux is comparable to the external input fluxes (10–60 % of the input; Fig. 9), the net circulation effect on the basin-wide isotope ratio is small. However, the net effect of circulation in the South Atlantic leads to a relatively strong import of ^{10}Be but only minor changes in ^{9}Be, and the deep-sea ^{10}Be/^{9}Be ratio becomes higher than the ratio of local external input in this basin (Fig. 6). In contrast, in the South Pacific, the net effect of circulation-related fluxes leads to a large import of ^{9}Be but a small export of ^{10}Be, and the deep-sea ^{10}Be/^{9}Be is much lower than the ratio in basin-wide external inputs (Fig. 6), consistent with a previous mass balance calculation (von Blanckenburg and Bouchez, 2014). In general, circulation can either add or remove Be isotopes from individual basins, but its net effect only makes the basin-wide isotope ratios deviate from those of basin-wide inputs to a relatively small extent, with its effect being largest in the South Pacific (Fig. 6).

4.3. Sensitivity analyses on oceanic ^{10}Be/^{9}Be ratios

Our analysis above has shown that the vertical profile of Be isotopes is mainly shaped by scavenging by POC and opal, and the inter-basin difference in Be isotope ratios is largely due to the difference in basin-wide external inputs, with the circulation effect playing a secondary role in the modern ocean. In a next step, the optimised model of Be cycling is used to develop intuition about how potential changes to the Be cycle, either via external sources or by internal cycling, would affect the seawater ^{10}Be/^{9}Be ratios in individual basins, in order to inform our expectations for how Earth system changes may be reflected in isotope records from marine sediments at seafloor.

4.3.1. Sensitivity to external sources

We first assess the response of ocean bottom ^{10}Be/^{9}Be ratios in the deep sea (>2 km) to changes in individual ^{9}Be sources. The ocean circulation is kept constant in all sensitivity analyses. The isotope response in two sub-basins, the North Atlantic and the North Pacific, is shown in Fig. 10. The benthic ^{9}Be flux on the continental shelves (2.9×10^{7} mol/yr) accounts for 43 % of the global ^{9}Be input, and thus a twofold increase in this source causes a large decrease in the basin-wide ^{10}Be/^{9}Be ratios, by 28–30 %. Over geological timescales, the variation in shelf benthic fluxes can be related to e.g., sea-level fluctuation and related expansion/shrinking of continental shelf area. In comparison, a twofold increase of riverine dissolved ^{9}Be flux globally, due to e.g., changes in continental denudation (von Blanckenburg and Bouchez, 2014), leads to an increase in the total ^{9}Be input by 28 %, and thus a decrease in the basin-wide ^{10}Be/^{9}Be ratios by 19–24 % (Fig. 10a-b). Finally, ^{10}Be/^{9}Be ratios in both sub-basins only decrease by 11 % for a twofold increase in the dust

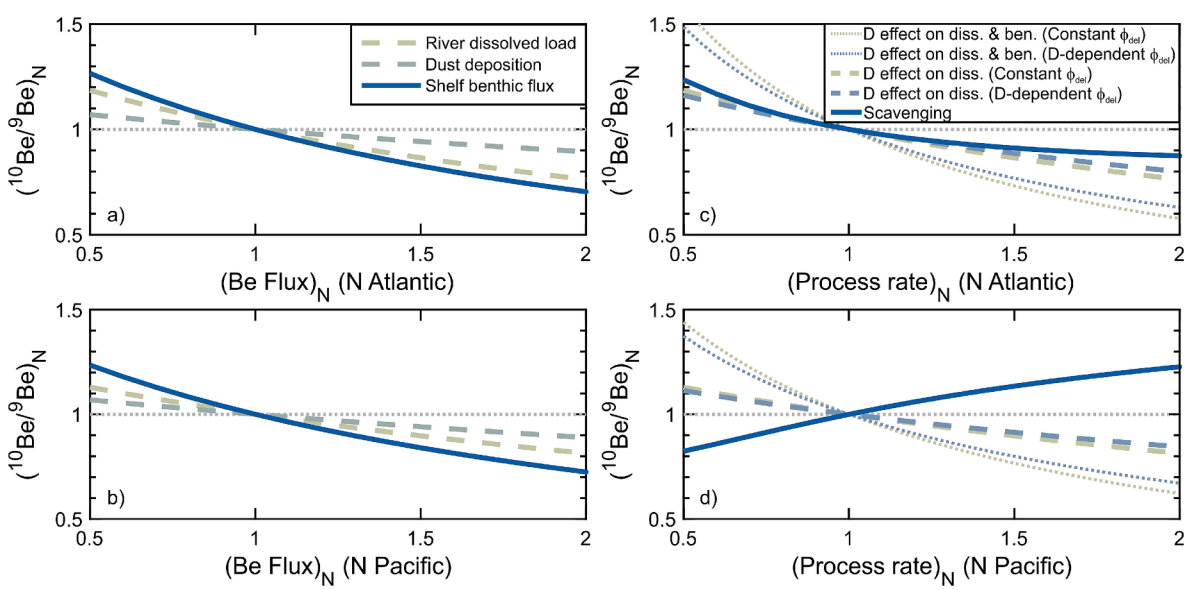

Fig. 10. Response of oceanic bottom ^{10}Be/^{9}Be ratios at depths of > 2 km to twofold changes in ^{9}Be inputs and in other key processes. Variables on the X-axis and Y-axis are normalised to the values from the optimised model under present-day conditions. Parameters shown in the ^{9}Be input (a-b) include riverine dissolved load, dust deposition, and benthic fluxes on continental shelves. The responses of ^{10}Be/^{9}Be ratios in the North Atlantic (a) and the North Pacific (b) are shown separately. For dust deposition, both ^{10}Be and ^{9}Be inputs change with dust depositional fluxes. Parameters controlling key processes (c-d) include continental denudation rate (D) and oceanic particle scavenging intensity (linearly correlated with sinking particulate flux). The four legends related to denudation indicate different scenarios (von Blanckenburg and Bouchez, 2014; von Blanckenburg et al., 2022; Deng et al., 2023) for the controls on the delivery efficiency of continent-derived ^{9}Be to the open ocean (ϕ_{del}). In each sensitivity analysis (each line), only the input flux or process indicated varies, and all other model parameters are kept the same as those in the optimised model (Scenario 10).

flux, which acts as a source for both ^{9}Be and ^{10}Be. Overall, the basin-wide ^{10}Be/^{9}Be ratios primarily respond to changes in benthic fluxes, due to their crucial role in the oceanic ^{9}Be budget.

4.3.2. Sensitivity to continental denudation

We here consider the effect of two key processes, including continental denudation and oceanic particle scavenging. Regarding continental denudation, its relationship with the effective continent-derived ^{9}Be input is still debated, due to incomplete understanding of ^{9}Be transfer through the land–ocean interface. As illustrated in von Blanckenburg et al. (2022), the delivery efficiency of continent-derived ^{9}Be across the land–ocean interface (ϕ_{del}) encompasses two components: the fraction of riverine dissolved ^{9}Be that escapes the coastal trap, and the fraction of sediment-bound ^{9}Be that dissolves at the margins and enters the open ocean. Our modern Be cycle model (Section 4.1) does not rely on any assumptions regarding the effect of denudation on ϕ_{del}; instead, the delivery efficiency values of riverine dissolved load and benthic sedimentary fluxes are explicitly constrained based on observational data for estuarine scavenging efficiency and pore-water release, respectively. However, in the geological past, how the ϕ_{del} for each pathway changed in response to continental denudation still requires further investigation.

Here, as a sensitivity analysis, different scenarios for the controls on ϕ_{del} are included. Note that we only adopt the assumptions on the ^{9}Be delivery process from previous studies, rather than the exact ϕ_{del} value. First, ϕ_{del} is assumed as a constant (von Blanckenburg and Bouchez, 2014), so that the continent-derived ^{9}Be input to the open ocean linearly increases with denudation rate (Scenario A). Here, a rise in denudation would lead to a proportional increase in riverine dissolved input and benthic flux given the constant ϕ_{del} of both pathways. Second (Scenario B), ϕ_{del} of continent-derived ^{9}Be can be assumed to be controlled by particle concentration in estuaries and is negatively correlated with denudation rate (von Blanckenburg et al., 2022): an increase in denudation would diminish the delivery efficiency for both pathways, resulting in a smaller increase in the ^{9}Be flux reaching the open ocean compared to that in Scenario A. A third model for estuarine ^{9}Be removal (Li et al., 2021) suggests that oceanic ^{10}Be/^{9}Be ratios could potentially be insensitive to denudation rates, although this model requires a specific parameterisation of the relationship between coastal particle concentration and sediment yield. Such a parameterisation does not fit with the global river observations (von Blanckenburg et al., 2022) and is not included here. Scenarios A and B are modelled based on the assumptions described in previous studies (von Blanckenburg and Bouchez, 2014; von Blanckenburg et al., 2022), and are plotted in Fig. 10 to allow for inter-study comparability. Specifically, both the effective riverine dissolved load and the pore-water release fluxes on shelves are regulated by the denudation rate and the total ^{9}Be input increases either linearly (A) or non-linearly (B) with it. Hence, a twofold increase of denudation rates can lead to a decrease in basin-wide ^{10}Be/^{9}Be ratios by 38–42 % in Scenario A with constant ϕ_{del} (Fig. 10c-d). In comparison, basin-wide ^{10}Be/^{9}Be ratios decrease by a slightly smaller magnitude (33–37 %) in response to the same denudation changes in Scenario B with D-dependent ϕ_{del}.

It must be emphasised, however, that the relationship between the marine benthic source and the continental denudation may not be straightforward, and the two could be temporally decoupled. For example, the benthic ^{9}Be fluxes only show a small variability on the Californian margin (10–20 %), despite a fivefold variability in sediment mass accumulation rates (Deng et al., 2023). Indeed, benthic fluxes can also be controlled by other oceanic processes such as water advection at the sediment–water interface or porewater Mn-Fe redox cycling (Deng et al., 2023). The evidence from the existing benthic ^{9}Be flux data suggests that the controls on the riverine dissolved load and on the marine benthic source may not be exactly the same. We thus consider two further scenarios (C-D), assuming that only the effective riverine dissolved ^{9}Be source responds to continental denudation following the parameterisation of Scenarios A-B (Fig. 10c-d). Accordingly, with a twofold increase in denudation rates, the response of oceanic ^{10}Be/^{9}Be to denudation rates is reduced overall relative to Scenarios A-B, but is once again larger in Scenario C (constant ϕ_{del}; 19–24 %) compared to Scenario D (D-dependent ϕ_{del}; 15–20 %). Likewise, with a 50 % decrease in denudation rates, the global-averaged deep-sea ^{10}Be/^{9}Be ratios increase by 13–48 %, depending on the chosen scenario (A-D).

4.3.3. Sensitivity to particle scavenging

We next examine sensitivity to internal cycling processes, i.e., scavenging by marine particles. Scavenging intensity is controlled by, and varies in proportion with, the flux of sinking biogenic particles (e.g., POC or opal). Even when input and output fluxes of Be isotopes are kept constant, modelled oceanic ^{10}Be/^{9}Be ratios respond to the scavenging intensity, and change in opposite directions between the Pacific and the Atlantic (Fig. 10c-d). For example, a decrease in scavenging intensity leads to an increase in the oceanic residence time of Be isotopes and a stronger effect of ocean circulation and mixing, such that the inter- and intra-basin gradients in ^{10}Be/^{9}Be ratios become smaller. A smaller inter-basin difference in response to weaker scavenging is also observed in simulations for other trace metals, such as Nd isotopes (Du et al., 2020; Robinson et al., 2023). In addition, if the lower particulate Be flux delivered to the seafloor leads to a decrease in benthic ^{9}Be input, an even longer Be residence time and a stronger homogenisation effect would result. Nevertheless, as mentioned above, the relationship between sedimentation rates and benthic fluxes cannot be readily inferred (Deng et al., 2023). Overall, a weaker scavenging intensity (by 50 %) can cause a higher ^{10}Be/^{9}Be ratio in the Atlantic (by 24 %) and a lower ratio in the Pacific (by 18 %; Fig. 10c-d).

4.4. Future research directions and implications for oceanic applications of Be isotopes

We have compiled constraints on the oceanic sources of Be isotopes with observations of their distribution in the global ocean to optimise a mechanistic Be cycling model. This optimisation tunes the scavenging efficiency of Be by particles, and though unconstrained, yields scavenging constants that are in line with observations. By integrating these independent constraints, our optimised model provides a consistent mechanistic view of the marine Be cycle and budget, and has allowed us to interrogate key controlling mechanisms. Nevertheless, several limitations remain in this modelling approach, and can be improved on in the future to provide better constraints on the key oceanic processes.

First, a mechanistic understanding of the environmental controls on individual Be sources, such as the riverine dissolved load and the marine benthic flux, is still required in order to model the spatio-temporal distribution of seawater Be isotopes with high accuracy. In particular, regarding the benthic ^{9}Be flux in the model, we invoke a simple parameterisation based on water depth for simplification, as supported by pore-water Be observations (Deng et al., 2023). This depth-dependence could reflect a combination of multiple processes, such as Mn-Fe redox cycling (Elrod et al., 2004; McManus et al., 2012), porewater-seawater exchange (Shi et al., 2019) and sediment accumulation (Middelburg et al., 1997), all of which can vary with water depth. In the future, a more mechanistic parameterisation of the benthic flux and its release timescale based on additional pore-water Be observations across ocean basins, together with modelling of early diagenesis (Du, 2023), will provide important insights into the controls on the oceanic Be cycle.

Second, to obtain a comprehensive parameterisation of the internal oceanic cycle of Be isotopes, more empirical data constraints are needed on the water-column scavenging processes for diverse particle types, particularly POC, opal and Mn oxides. Although our optimised scavenging constants fall within the range of limited observations (Section 3.1), these constants could also be prescribed in our model if their representative values, uncertainties and controls are better constrained

in the future. In addition, the distribution of particulate Mn oxides is still poorly constrained (van Hulten et al., 2017), impeding a rigorous assessment of its effect on Be scavenging. Recent studies show that Mn oxides are the dominant scavenging agent for particle-reactive Nd (Haley et al., 2021; Du et al., 2022). Although Be may not respond to scavenging by Mn oxides to the same extent (Balistrieri and Murray, 1986; Anderson et al., 1990), a detailed water-column Mn oxide dataset with a higher spatial resolution would nonetheless help to better constrain its role compared to other particle types.

Third, the ocean circulation transport matrix can be improved with better data constraints. The circulation in the Arctic is sensitive to short-term and regional-scale changes (Charette et al., 2020) given its small volume, and is less constrained compared to other basins (DeVries and Primeau, 2011). Hence, the relatively large model-observation mismatch in the Arctic can potentially be reduced with the support of a better-constrained regional circulation.

Our data-constrained model of Be isotope cycling also has potential implications for the wide applications of Be isotopes in the oceans, such as reconstruction of paleo-geomagnetic intensity and ^{10}Be production rate (Christl et al., 2010; Savranskaia et al., 2021), paleo-archive dating (Bourlès et al., 1989b), and tracking continental inputs (Willenbring and von Blanckenburg, 2010). Changes in scavenging intensity and external sources, in response to paleo-environmental variations, can introduce additional uncertainties to these applications. Such effects should be taken into account in the future and can be quantified using a modelling approach similar to that taken in our study. Additionally, the time-resolved records of inter-basin differences in ^{10}Be/^{9}Be ratios (e.g., North Pacific vs. North Atlantic) may be utilised to reconstruct internal cycling processes if the source magnitudes of Be isotopes are constant or can be constrained independently during a given time period. A smaller inter-basin isotope difference could hint at a stronger homogenisation of oceanic Be, driven either by a more vigorous deep-water circulation or by weaker particle scavenging (Fig. 10c-d).

5. Conclusions

We present a three-dimensional model of the cycling of Be isotopes in the modern ocean, constrained by a compilation of input fluxes and water column observations. This model reproduces the observed distributions of the individual isotopes as well as ^{10}Be/^{9}Be ratios over ~ 100-fold variability (10^{-8}-10^{-6} atoms/atoms). In comparison, previous mass balance models were only able to calculate sub-basin-averaged isotope ratios (~10-fold variability). Our model further revisits the effects of individual sources, scavenging and circulation, and quantifies the sensitivity of seawater ^{10}Be/^{9}Be ratios to key continental-oceanic processes.

(1) The spatial distribution of seawater Be isotopes is primarily shaped by both basin-wide external inputs and scavenging processes. The major source of ^{10}Be is atmospheric wet deposition (96 % of the total), while the marine benthic flux is the major source of ^{9}Be (54 % of the total). Our model optimisation emphasises that the scavenging agents dominating the sinking Be flux on the global scale are particulate organic carbon and opal (~90 % on average).

(2) Circulation can add (or remove) both Be isotopes into (from) the dissolved reservoir of individual basins, but the magnitude of these circulation-related fluxes is smaller (~0–60 %) than external inputs, except in the South Pacific. The basin-wide ^{10}Be/^{9}Be ratios in deep waters thus largely reflect those of external inputs in most basins, because the net transport flux is either small or bears an isotope ratio that is similar to the external inputs.

(3) Basin-wide ^{10}Be/^{9}Be ratios are sensitive to several Earth system processes. With a 50 % decrease in denudation rates, deep-ocean ^{10}Be/^{9}Be ratios increase non-linearly, by 13 to 48 %. With a 50 % decrease in scavenging intensity and the resulting stronger effect of circulation mixing, the isotope response differs between basins, with an increase in ^{10}Be/^{9}Be ratios in the North Atlantic (by 24 %) and a decrease in the North Pacific (by 18 %), resulting in a smaller inter-basin gradient.

CRediT authorship contribution statement

Kai Deng: Writing – original draft, Visualization, Methodology, Formal analysis, Conceptualization. **Gregory F. de Souza:** Writing – review & editing, Methodology. **Jianghui Du:** Writing – review & editing, Methodology.

Data availbility

Data is available through Zenodo at https://doi.org/10.5281/zenodo.12596171; The AWESOME model code is available through Github at https://github.com/MTEL-USC/AWESOME-OCIM. Code files related to Be-specific processes are available at https://doi.org/10.5281/zenodo.13888373.

Declaration of competing interest

The authors declare that they have no known competing financial interests or personal relationships that could have appeared to influence the work reported in this paper.

Acknowledgments

K.D. acknowledges support through ETH Zurich Postdoctoral Fellowship 20-1 FEL-24 and National Key R&D Program of China (no. 2022YFF0800504). G.F.dS. is supported by ETH Zurich. J.D. is supported by The Fundamental Research Funds for the Central Universities, Peking University. We thank Derek Vance and Friedhelm von Blanckenburg for discussion of earlier versions of this manuscript, and thank Hengdi Liang for discussions of the AWESOME model.

Appendix A. Supplementary material

Supplementary Material includes Supplementary Text and Figures 1–5. Supplementary Text describes the parameterisation of a potential benthic ^{10}Be source in the sensitivity test. Figure S1 shows the depth profiles of particle concentrations for major particle types. Figure S2 shows modelled vs. observed water-column particulate Mn oxide. Figure S3 shows depth profiles of modelled Be isotopes derived from different kinds of scavenging parameters. Figure S4 shows the comparison between observed and modelled depth profiles of dissolved ^{10}Be/^{9}Be in the Atlantic and the Pacific. Figure S5 shows the global distribution of modelled seawater ^{10}Be/^{9}Be ratios. Supplementary material to this article can be found online at https://doi.org/10.1016/j.gca.2024.10.025.

References

Abbott, A.N., Haley, B.A., McManus, J., Reimers, C.E., 2015. The sedimentary flux of dissolved rare earth elements to the ocean. Geochim. Cosmochim. Acta 154, 186–200.

Amante, C., Eakins, B., 2009. ETOPO1 1 Arc-Minute Global Relief Model: Procedures, Data Sources and Analysis, National Geophysical Data Center, NESDIS, NOAA. US Dept, Commerce, Boulder, CO, USA.

Anderson, R.F., Lao, Y., Broecker, W.S., Trumbore, S.E., Hofmann, H.J., Wolfli, W., 1990. Boundary scavenging in the Pacific Ocean: a comparison of10Be and231Pa. Earth Planet. Sci. Lett. 96 (3), 287–304.

Aumont, O., Éthé, C., Tagliabue, A., Bopp, L., Gehlen, M., 2015. PISCES-v2: an ocean biogeochemical model for carbon and ecosystem studies. Geoscientific Model Development 8 (8), 2465–2513.

Bacon, M.P., Anderson, R.F., 1982. Distribution of thorium isotopes between dissolved and particulate forms in the deep sea. Journal of Geophysical Research: Oceans 87 (C3), 2045–2056.

Balistrieri, L.S., Murray, J.W., 1986. The surface chemistry of sediments from the Panama Basin: The influence of Mn oxides on metal adsorption. Geochim. Cosmochim. Acta 50 (10), 2235–2243.

Belmaker, R., Lazar, B., Tepelyakov, N., Stein, M., Beer, J., 2008. 10Be in Lake Lisan sediments — A proxy for production or climate? Earth Planet. Sci. Lett. 269 (3), 448–457.
Bourlès, D.L., Klinkhammer, G., Campbell, A.C., Measures, C.I., Brown, E.T., Edmond, J. M., 1989b. Beryllium in marine pore waters: geochemical and geochronological implications. Nature 341 (6244), 731–733.
Bourlès, D., Raisbeck, G.M., Yiou, F., 1989a. 10Be and 9Be in marine sediments and their potential for dating. Geochim. Cosmochim. Acta 53 (2), 443–452.
Brown, E.T., Measures, C.I., Edmond, J.M., Bourlès, D.L., Raisbeck, G.M., Yiou, F., 1992. Continental inputs of beryllium to the oceans. Earth Planet. Sci. Lett. 114 (1), 101–111.
Bundy, R.M., Tagliabue, A., Hawco, N.J., Morton, P.L., Twining, B.S., Hatta, M., Noble, A.E., Cape, M.R., John, S.G., Cullen, J.T., Saito, M.A., 2020. Elevated sources of cobalt in the Arctic Ocean. Biogeosciences 17 (19), 4745–4767.
Charette, M.A., Kipp, L.E., Jensen, L.T., Dabrowski, J.S., Whitmore, L.M., Fitzsimmons, J. N., Williford, T., Ulfsbo, A., Jones, E., Bundy, R.M., Vivancos, S.M., Pahnke, K., John, S.G., Xiang, Y., Hatta, M., Petrova, M.V., Heimbürger-Boavida, L.-E., Bauch, D., Newton, R., Pasqualini, A., Agather, A.M., Amon, R.M.W., Anderson, R.F., Andersson, P.S., Benner, R., Bowman, K.L., Edwards, R.L., Gdaniec, S., Gerringa, L.J. A., González, A.G., Granskog, M., Haley, B., Hammerschmidt, C.R., Hansell, D.A., Henderson, P.B., Kadko, D.C., Kaiser, K., Laan, P., Lam, P.J., Lamborg, C.H., Levier, M., Li, X., Margolin, A.R., Measures, C., Middag, R., Millero, F.J., Moore, W. S., Paffrath, R., Planquette, H., Rabe, B., Reader, H., Rember, R., Rijkenberg, M.J.A., Roy-Barman, M., Rutgers van der Loeff, M., Saito, M., Schauer, U., Schlosser, P., Sherrell, R.M., Shiller, A.M., Slagter, H., Sonke, J.E., Stedmon, C., Woosley, R.J., Valk, O., van Ooijen, J., Zhang, R., 2020. The Transpolar Drift as a Source of Riverine and Shelf-Derived Trace Elements to the Central Arctic Ocean. Journal of Geophysical Research: Oceans 125 (5), e2019JC015920.
Chase, Z., Anderson, R.F., Fleisher, M.Q., Kubik, P.W., 2002. The influence of particle composition and particle flux on scavenging of Th, Pa and Be in the ocean. Earth Planet. Sci. Lett. 204 (1), 215–229.
Chien, C.-T., Mackey, K.R.M., Dutkiewicz, S., Mahowald, N.M., Prospero, J.M., Paytan, A., 2016. Effects of African dust deposition on phytoplankton in the western tropical Atlantic Ocean off Barbados. Global Biogeochem. Cycles 30 (5), 716–734.
Chmeleff, J., von Blanckenburg, F., Kossert, K., Jakob, D., 2010. Determination of the 10 Be half-life by multicollector ICP-MS and liquid scintillation counting. Nucl. Instrum. Methods Phys. Res., Sect. B 268 (2), 192–199.
Christl, M., Lippold, J., Steinhilber, F., Bernsdorff, F., Mangini, A., 2010. Reconstruction of global 10Be production over the past 250ka from highly accumulating Atlantic drift sediments. Quat. Sci. Rev. 29 (19), 2663–2672.
Dale, A.W., Nickelsen, L., Scholz, F., Hensen, C., Oschlies, A., Wallmann, K., 2015. A revised global estimate of dissolved iron fluxes from marine sediments. Global Biogeochem. Cycles 29 (5), 691–707.
Deng, K., Wittmann, H., von Blanckenburg, F., 2020. The depositional flux of meteoric cosmogenic 10Be from modeling and observation. Earth Planet. Sci. Lett. 550, 116530.
Deng, K., Yang, S., Du, J., Lian, E., Vance, D., 2022. Dominance of benthic flux of REEs on continental shelves: implications for oceanic budgets. Geochemical Perspectives Letters 22, 26–30.
Deng, K., Rickli, J., Suhrhoff, T.J., Du, J., Scholz, F., Severmann, S., Yang, S., McManus, J., Vance, D., 2023. Dominance of benthic fluxes in the oceanic beryllium budget and implications for paleo-denudation records. Science Advances 9 (23), eadg3702.
DeVries, T., 2014. The oceanic anthropogenic CO2 sink: Storage, air-sea fluxes, and transports over the industrial era. Global Biogeochem. Cycles 28 (7), 631–647.
DeVries, T., Primeau, F., 2011. Dynamically and Observationally Constrained Estimates of Water-Mass Distributions and Ages in the Global Ocean. Journal of Physical Oceanography 41 (12), 2381–2401.
Du, J., 2023. SedTrace 1.0: a Julia-based framework for generating and running reactive-transport models of marine sediment diagenesis specializing in trace elements and isotopes. Geosci. Model Dev. 16 (20), 5865–5894.
Du, J., Haley, B.A., Mix, A.C., 2020. Evolution of the Global Overturning Circulation since the Last Glacial Maximum based on marine authigenic neodymium isotopes. Quat. Sci. Rev. 241, 106396.
Du, J., Haley, B.A., Mix, A.C., Abbott, A.N., McManus, J., Vance, D., 2022. Reactive-transport modeling of neodymium and its radiogenic isotope in deep-sea sediments: The roles of authigenesis, marine silicate weathering and reverse weathering. Earth Planet. Sci. Lett. 596, 117792.
Duce, R.A., Liss, P.S., Merrill, J.T., Atlas, E.L., Buat-Menard, P., Hicks, B.B., Miller, J.M., Prospero, J.M., Arimoto, R., Church, T.M., Ellis, W., Galloway, J.N., Hansen, L., Jickells, T.D., Knap, A.H., Reinhardt, K.H., Schneider, B., Soudine, A., Tokos, J.J., Tsunogai, S., Wollast, R., Zhou, M., 1991. The atmospheric input of trace species to the world ocean. Global Biogeochem. Cycles 5 (3), 193–259.
Eisenring, C., Oliver, S.E., Khatiwala, S., de Souza, G.F., 2022. Influence of GEOTRACES data distribution and misfit function choice on objective parameter retrieval in a marine zinc cycle model. Biogeosciences 19 (21), 5079–5106.
Elrod, V.A., Berelson, W.M., Coale, K.H., Johnson, K.S., 2004. The flux of iron from continental shelf sediments: A missing source for global budgets. Geophys. Res. Lett. 31 (12).
Frank, M., O'Nions, R.K., Hein, J.R., Banakar, V.K., 1999. 60 Myr records of major elements and Pb–Nd isotopes from hydrogenous ferromanganese crusts: reconstruction of seawater paleochemistry. Geochim. Cosmochim. Acta 63 (11), 1689–1708.
Frank, M., Rutgers van der Loeff, M.M., Kubik, P.W., Mangini, A., 2002. Quasi-conservative behaviour of 10Be in deep waters of the Weddell Sea and the Atlantic sector of the Antarctic Circumpolar Current. Earth Planet. Sci. Lett. 201 (1), 171–186.
Frank, M., Porcelli, D., Andersson, P., Baskaran, M., Björk, G., Kubik, P.W., Hattendorf, B., Guenther, D., 2009. The dissolved Beryllium isotope composition of the Arctic Ocean. Geochim. Cosmochim. Acta 73 (20), 6114–6133.
Gaillardet, J., Lemarchand, D., 2018. Boron in the Weathering Environment. In: Marschall, H., Foster, G. (Eds.), Boron Isotopes: the Fifth Element. Springer International Publishing, Cham, pp. 163–188.
GEOTRACES Intermediate Data Product Group, 2021. The GEOTRACES Intermediate Data Product 2021 (IDP2021). NERC EDS British Oceanographic Data Centre NOC.
Grenier, M., van Beek, P., Lerner, P., Sanial, V., Souhaut, M., Lagarde, M., Marchal, O., Reyss, J.L., 2023. New insights on the 7Be cycle in the ocean. Deep Sea Res. Part I 194, 103967.
Haley, B.A., Wu, Y., Muratli, J.M., Basak, C., Pena, L.D., Goldstein, S.L., 2021. Rare earth element and neodymium isotopes of the eastern US GEOTRACES Equatorial Pacific Zonal Transect (GP16). Earth Planet. Sci. Lett. 576, 117233.
Heikkilä, U., Beer, J., Abreu, J.A., Steinhilber, F., 2013. On the Atmospheric Transport and Deposition of the Cosmogenic Radionuclides (10 Be): A Review. Space Sci. Rev. 176 (1), 321–332.
Heikkilä, U., von Blanckenburg, F., 2015. The global distribution of Holocene meteoric 10Be fluxes from atmospheric models. Distribution maps for terrestrial Earths surface applications, GFZ Data Services, GFZ Potsdam, Germany.
Jeandel, C., 2016. Overview of the mechanisms that could explain the 'Boundary Exchange' at the land-ocean contact. Philosophical Transactions of the Royal Society a-Mathematical Physical and Engineering Sciences 374 (2081).
John, S.G., Liang, H., Weber, T., DeVries, T., Primeau, F., Moore, K., Holzer, M., Mahowald, N., Gardner, W., Mishonov, A., Richardson, M.J., Faugere, Y., Taburet, G., 2020. AWESOME OCIM: A simple, flexible, and powerful tool for modeling elemental cycling in the oceans. Chem. Geol. 533, 119403.
Khatiwala, S., Primeau, F., Holzer, M., 2012. Ventilation of the deep ocean constrained with tracer observations and implications for radiocarbon estimates of ideal mean age. Earth Planet. Sci. Lett. 325–326, 116–125.
Kong, W.Y., Zhou, L.P., 2021. Tracing Water Masses and Assessing Boundary Scavenging Intensity With Beryllium Isotopes in the Northern South China Sea. Journal of Geophysical Research: Oceans 126 (7), e2021JC017236.
Kretschmer, S., Geibert, W., Rutgers van der Loeff, M.M., Schnabel, C., Xu, S., Mollenhauer, G., 2011. Fractionation of 230Th, 231Pa, and 10Be induced by particle size and composition within an opal-rich sediment of the Atlantic Southern Ocean. Geochim. Cosmochim. Acta 75 (22), 6971–6987.
Ku, T.L., Kusakabe, M., Measures, C.I., Southon, J.R., Cusimano, G., Vogel, J.S., Nelson, D.E., Nakaya, S., 1990. Beryllium isotope distribution in the western North Atlantic: a comparison to the Pacific. Deep Sea Research Part a. Oceanographic Research Papers 37 (5), 795–808.
Kusakabe, M., Ku, T.L., Vogel, J., Southon, J.R., Nelson, D.E., Richards, G., 1982. 10Be profiles in seawater. Nature 299 (5885), 712–714.
Kusakabe, M., Ku, T.L., Southon, J.R., Vogel, J.S., Nelson, D.E., Measures, C.I., Nozaki, Y., 1987. Distribution of10Be and9Be in the Pacific Ocean. Earth Planet. Sci. Lett. 82 (3), 231–240.
Kusakabe, M., Ku, T.L., Southon, J.R., Measures, C.I., 1990. Beryllium isotopes in the ocean. Geochem. J. 24 (4), 263–272.
Lacan, F., Jeandel, C., 2005. Neodymium isotopes as a new tool for quantifying exchange fluxes at the continent–ocean interface. Earth Planet. Sci. Lett. 232 (3), 245–257.
Lam, P.J., Lee, J.-M., Heller, M.I., Mehic, S., Xiang, Y., Bates, N.R., 2018. Size-fractionated distributions of suspended particle concentration and major phase composition from the U.S. GEOTRACES Eastern Pacific Zonal Transect (GP16). Mar. Chem. 201, 90–107.
Li, Y.-H., 2005. Controversy over the relationship between major components of sediment-trap materials and the bulk distribution coefficients of 230Th, 231Pa, and 10Be. Earth Planet. Sci. Lett. 233 (1), 1–7.
Li, S., Goldstein, S.L., Raymo, M.E., 2021. Neogene continental denudation and the beryllium conundrum. Proceedings of the National Academy of Sciences 118 (42), e2026456118.
McManus, J., Berelson, W.M., Severmann, S., Johnson, K.S., Hammond, D.E., Roy, M., Coale, K.H., 2012. Benthic manganese fluxes along the Oregon-California continental shelf and slope. Cont. Shelf Res. 43, 71–85.
Measures, C.I., Edmond, J.M., 1982. Beryllium in the water column of the central North Pacific. Nature 297 (5861), 51–53.
Measures, C.I., Edmond, J.M., 1983. The geochemical cycle of 9Be: a reconnaissance. Earth Planet. Sci. Lett. 66, 101–110.
Measures, C.I., Ku, T.L., Luo, S., Southon, J.R., Xu, X., Kusakabe, M., 1996. The distribution of 10Be and 9Be in the South Atlantic. Deep Sea Res. Part I 43 (7), 987–1009.
Merrill, J.R., Lyden, E.F.X., Honda, M., Arnold, J.R., 1960. The sedimentary geochemistry of the beryllium isotopes. Geochim. Cosmochim. Acta 18 (1), 108–129.
Middelburg, J.J., Soetaert, K., Herman, P.M.J., 1997. Empirical relationships for use in global diagenetic models. Deep Sea Res. Part I 44 (2), 327–344.
Milliman, J.D., Farnsworth, K.L., 2011. River Discharge to the Coastal Ocean – A Global Synthesis. Cambridge University Press.
Pasquier, B., Hines, S.K.V., Liang, H., Wu, Y., Goldstein, S.L., John, S.G., 2022. GNOM v1.0: an optimized steady-state model of the modern marine neodymium cycle. Geosci. Model Dev. 15 (11), 4625–4656.
Raisbeck, G.M., Yiou, F., Fruneau, M., Loiseaux, J.M., Lieuvin, M., 1979. 10Be concentration and residence time in the ocean surface layer. Earth Planet. Sci. Lett. 43 (2), 237–240.
Robinson, S., Ivanovic, R.F., Gregoire, L.J., Tindall, J., van de Flierdt, T., Plancherel, Y., Pöppelmeier, F., Tachikawa, K., Valdes, P.J., 2023. Simulating marine neodymium

isotope distributions using Nd v1.0 coupled to the ocean component of the FAMOUS–MOSES1 climate model: sensitivities to reversible scavenging efficiency and benthic source distributions. Geosci. Model Dev. 16 (4), 1231–1264.
Rudnick, R.L., Gao, S., 2003. 3.01 - Composition of the Continental Crust A2 - Holland, Heinrich D. In: Turekian, K.K. (Ed.), Treatise on Geochemistry. Pergamon, Oxford, pp. 1–64.
Savranskaia, T., Egli, R., Valet, J.-P., Bassinot, F., Meynadier, L., Bourlès, D.L., Simon, Q., Thouveny, N., 2021. Disentangling magnetic and environmental signatures of sedimentary 10Be/9Be records. Quat. Sci. Rev. 257, 106809.
Segl, M., Mangini, A., Beer, J., Bonani, G., Suter, M., Wölfli, W., Measures, C., 1987. 10Be in the Atlantic ocean, a transect at 25° N. Nucl. Instrum. Methods Phys. Res., Sect. B 29 (1), 332–334.
Shen, C., Beer, J., Kubik, P., Sun, W., Liu, T., Liu, K., 2010. 10Be in desert sands, falling dust and loess in China. Nucl. Instrum. Methods Phys. Res., Sect. B 268 (7–8), 1050–1053.
Shi, X., Wei, L., Hong, Q., Liu, L., Wang, Y., Shi, X., Ye, Y., Cai, P., 2019. Large benthic fluxes of dissolved iron in China coastal seas revealed by 224Ra/228Th disequilibria. Geochim. Cosmochim. Acta 260, 49–61.
Siddall, M., Khatiwala, S., van de Flierdt, T., Jones, K., Goldstein, S.L., Hemming, S., Anderson, R.F., 2008. Towards explaining the Nd paradox using reversible scavenging in an ocean general circulation model. Earth Planet. Sci. Lett. 274 (3), 448–461.
Simon, Q., Thouveny, N., Bourlès, D.L., Nuttin, L., Hillaire-Marcel, C., St-Onge, G., 2016. Authigenic 10 Be/ 9 Be ratios and 10 Be-fluxes (230 Th xs -normalized) in central Baffin Bay sediments during the last glacial cycle: Paleoenvironmental implications. Quat. Sci. Rev. 140, 142–162.
Simon, Q., Thouveny, N., Bourlès, D.L., Bassinot, F., Savranskaia, T., Valet, J.-P., 2018. Increased production of cosmogenic 10Be recorded in oceanic sediment sequences: Information on the age, duration, and amplitude of the geomagnetic dipole moment minimum over the Matuyama-Brunhes transition. Earth Planet. Sci. Lett. 489, 191–202.
Suhrhoff, T.J., Rickli, J., Crocket, K., Bura-Nakic, E., Vance, D., 2019. Behavior of beryllium in the weathering environment and its delivery to the ocean. Geochim. Cosmochim. Acta 265, 48–68.
Thiele, G., Sarmiento, J., 1990. Tracer dating and ocean ventilation. Journal of Geophysical Research: Oceans 95 (C6), 9377–9391.
van Hulten, M., Middag, R., Dutay, J.C., de Baar, H., Roy-Barman, M., Gehlen, M., Tagliabue, A., Sterl, A., 2017. Manganese in the west Atlantic Ocean in the context of the first global ocean circulation model of manganese. Biogeosciences 14 (5), 1123–1152.
van Hulten, M., Dutay, J.C., Roy-Barman, M., 2018. A global scavenging and circulation ocean model of thorium-230 and protactinium-231 with improved particle dynamics (NEMO–ProThorP 0.1). Geosci. Model Dev. 11 (9), 3537–3556.
von Blanckenburg, F., Bouchez, J., 2014. River fluxes to the sea from the ocean's Be-10/Be-9 ratio. Earth Planet. Sci. Lett. 387, 34–43.
von Blanckenburg, F., Igel, H., 1999. Lateral mixing and advection of reactive isotope tracers in ocean basins: observations and mechanisms. Earth Planet. Sci. Lett. 169 (1), 113–128.
von Blanckenburg, F., O'Nions, R.K., Belshaw, N.S., Gibb, A., Hein, J.R., 1996. Global distribution of beryllium isotopes in deep ocean water as derived from Fe-Mn crusts. Earth Planet. Sci. Lett. 141 (1), 213–226.
von Blanckenburg, F., Bouchez, J., Ibarra, D.E., Maher, K., 2015. Stable runoff and weathering fluxes into the oceans over Quaternary climate cycles. Nat. Geosci. 8, 538–542.
von Blanckenburg, F., Bouchez, J., Willenbring, J.K., Ibarra, D.E., Rugenstein, J.K.C., 2022. There is no Neogene denudation conundrum. Proceedings of the National Academy of Sciences 119 (35), e2202387119.
Wang, C., von Blanckenburg, F., Lian, E., Yang, S., Perez, J.P.H., Wittmann, H., 2024. River-to-ocean pathways of beryllium-9 through estuaries. Geochim. Cosmochim. Acta 370, 89–103.
Weber, T., John, S., Tagliabue, A., DeVries, T., 2018. Biological uptake and reversible scavenging of zinc in the global ocean. Science 361 (6397), 72–76.
Willenbring, J.K., von Blanckenburg, F., 2010. Long-term stability of global erosion rates and weathering during late-Cenozoic cooling. Nature 465 (7295), 211–214.
Wittmann, H., von Blanckenburg, F., Mohtadi, M., Christl, M., Bernhardt, A., 2017. The competition between coastal trace metal fluxes and oceanic mixing from the 10Be/9Be ratio: Implications for sedimentary records. Geophys. Res. Lett. 44 (16), 8443–8452.
Xu, X., 1994. Geochemical studies of beryllium isotopes in marine and continental natural water systems. University of Southern California.
Yang, W., Guo, L., Chuang, C.-Y., Santschi, P.H., Schumann, D., Ayranov, M., 2015. Influence of organic matter on the adsorption of 210Pb, 210Po and 7Be and their fractionation on nanoparticles in seawater. Earth Planet. Sci. Lett. 423, 193–201.
Yi, L., Medina-Elizalde, M., Kletetschka, G., Yao, H., Simon, Q., Paterson, G.A., Bourlès, D.L., Deng, X., Du, J., Qin, H., Chen, Y., Xie, Q., Xiao, J., Wang, Y., Andreucci, C., Keddadouche, K., Aumaître, G., Liu, Y., Wang, H., Shen, Z., Gu, X., Smith, T., Dang, H., Jian, Z., Song, T., He, H., Deng, C., Zhu, R., 2020. The Potential of Marine Ferromanganese Nodules From Eastern Pacific as Recorders of Earth's Magnetic Field Changes During the Past 4.7 Myr: A Geochronological Study by Magnetic Scanning and Authigenic 10Be/9Be Dating. Journal of Geophysical Research: Solid Earth 125 (7), e2019JB018639.
You, C.F., Lee, T., Li, Y.H., 1989. The partition of Be between soil and water. Chem. Geol. 77 (2), 105–118.